Parabolic resolvent modes for streaky structures in transitional and turbulent boundary layers

Kenzo Sasaki [1], André V. G. Cavalieri [2], Ardeshir Hanifi [1], and Dan S. Henningson [1]
[1] *FLOW, KTH Engineering Mechanics, Royal Institute of Technology, SE-100 44 Stockholm, Sweden*
[2] *Divisão de Engenharia Aeronáutica, Instituto Tecnológico de Aeronáutica (ITA), Aerodynamics Department, 12228-900, São José dos Campos, Brazil*

(Received 15 April 2022; accepted 26 July 2022; published 27 October 2022)

Resolvent analysis has found applications in several areas of fluid mechanics, providing physical insight into both laminar and turbulent flows. In spite of such fact, the global (3D) resolvent is computationally expensive, which limits the size of the domain and the Reynolds number of the flows which can be considered. In this work, we derive a parabolic resolvent approach, which enables a significant increase in the computational efficiency of the calculation, for streaky structures in boundary layer flows. The computational speedup depends on the size of the problem and could be of more than one order of magnitude for the same accuracy as the global calculation. The method is derived based on an optimization method via the Lagrange multipliers over the linearized boundary layer equations and it is coupled to a Krylov-Arnoldi decomposition to the computation of suboptimals. The application of the method is exemplified for two problems: a Falkner-Skan boundary layer, where we obtain trends for both the optimals and suboptimals, and a turbulent boundary layer, where characteristics such as the double peak in the spectrum and the characteristic inner and outer length scales can be recovered when a variable eddy viscosity is considered. In both cases, a scaling is found for the dominant gain, given in terms of the fourth power of the Reynolds number, defined in terms of the relevant scale for the problem, the displacement thickness, and the modified Rotta-Clauser parameter for the laminar and turbulent boundary layers, respectively. For the laminar case, we further demonstrate that a forcing limited to the free-stream region is capable of generating streaky structures inside the boundary layer, a relevant feature for free-stream turbulence-induced transition.

DOI: 10.1103/PhysRevFluids.7.104611

I. INTRODUCTION

Resolvent analysis is based on an input-output formulation, derived in the frequency domain, which has become of frequent use for several different applications in the fluid mechanics community, both for laminar-transitional and turbulent flows. The basic idea consists in performing a Reynolds decomposition of flow variables and replacing the terms of the Navier-Stokes (NS) equations that are nonlinear in fluctuations by a forcing term to an otherwise linear operator [1–3]. Such nonlinear forcing is treated as an unknown and the most amplified flow responses (outputs) to such forcings (inputs) are sought. Given the non-normality of the NS operator [4–8], which leads to

strong transient amplifications of the flow fluctuations, relevant flow features may be extracted from this approach.

As an example, these optimal response modes of the resolvent operator may be used to deduce the coherent structures in the flow. Recent works [9,10] have shown that, when the forcing corresponds to white noise in the spatial direction, the optimal response modes of the resolvent operator correspond to the spectral proper orthogonal decomposition (SPOD) modes. This result has been used in several other applications for turbulent flows, where one could cite, for example, Refs. [9,11] for a turbulent jet, Refs. [1,3,12] for channel and pipe flows, Ref. [13] for a boundary layer, among others. The resolvent approach has also been used for active control [14] and estimation [15–17] of fluctuations and to extract the forcing statistics [18,19] in turbulent flows. A global resolvent approach has been recently used in a streamwise varying flow to better understand the nozzle dynamics in a turbulent jet [20].

The resolvent method along with other approaches, such as transient growth, are also of importance for applications in laminar-transitional flows, particularly due to the bypass transition induced via free-stream turbulence (FST) [21–25]. FST leads to the appearance of elongated streaky structures, with alternating high and low streamwise velocity fluctuations with respect to the base flow [26,27]. References [28–30], for example, show that the optimal perturbation, in this case obtained from a transient growth analysis, compares well with the FST-induced structures and may be used to boundary layer transition predictions. This has been used in Ref. [31] to improve the effectiveness of a closed-loop control scheme.

Calculation of resolvent modes for a parallel flow is straightforward, given its low computational cost, and may be found, for example, in Refs. [32,33]. For the global, three-dimensional case, different methods may be found in the literature. The effect of the resolvent operator can be determined by solving a linear system by means of an linear upper (LU) factorization iteratively as in Refs. [34,35]. Matrix-free, power-iteration schemes using the direct-adjoint equations are faster computationally and have been applied in Refs. [36–38] via a generalized minimal residual method to solve the linear system and in Ref. [39], which further computed suboptimal modes via the application of a Krylov-Arnoldi decomposition. A further approach would consist of a parabolization of the direct-adjoint optimization equations, as in Ref. [7]. Along these lines, the parabolized direct-adjoint iterations have been used in several works for the computation of optimal perturbations, such as Refs. [29,40,41] for Blasius, Falkner-Skan-Cooke, and compressible boundary layers and in Refs. [42,43] for a supersonic jet by means of an one-way Navier-Stokes approach which has the caveat of leading to a larger system. Finally, Ref. [44] applied a randomized approach for handling the operator of a high-Reynolds-number turbulent flow.

In the class of matrix-free methods, an interesting approach may be found in Ref. [45] where, similar to this work, a variational approach is used to estimate resolvent modes. In that approach, the Euler-Lagrange equations are expanded in a convenient basis, which eliminates the need to perform a matrix inversion (or LU decomposition), with the added advantage of avoiding the computation of the adjoint equations and permitting the calculation of the resolvent for any frequency. For the case evaluated in the work, the computational gains, when compared to the global calculation based on an LU decomposition, are of one order of magnitude, with an accompanying reduction of 40–75% in memory usage, with the caveat that the forcing reconstruction may deviate from the global calculation, depending on the case.

In the current work, we build on the matrix-free methods using the direct-adjoint boundary layer equations, setting the problem in terms of a global optimization for the forcing. In this work, we focus on the resolvent analysis of elongated streaky structures, which have null frequency and streamwise wave number, as it leads directly to a parabolic system [29]. For this case, the use of a spatial marching is straightforward, without the need to use an auxiliary condition, as in the parabolized stability equations [46], and without increasing the size of the problem, as in the one-way Euler and Navier-Stokes equations. We further apply the Krylov-Arnoldi decomposition to the calculation of suboptimal modes. This results in a method which is very efficient computationally and therefore allows application to large domains in the wall-normal and streamwise directions.

Two problems are studied for the application of the parabolic resolvent, both of which benefit from its low computational cost which enables large domains to be considered. This first one is a laminar boundary layer with pressure gradient (Falkner-Skan profile); This choice is motivated by the fact that even though this problem has been extensively studied in terms of the optimal perturbation (or initial condition), as in the works cited herein, not much is available in the literature in terms of the optimal forcing, particularly for higher Reynolds numbers and different favorable and adverse pressure gradients. Due to its low computational cost, the present parabolic resolvent method allows a thorough parametric characterization of the global input-output behavior of streaks in laminar boundary layers with pressure gradient. Furthermore, optimal forcing computations are of relevance for free-stream turbulence transition as the receptivity mechanisms are yet unclear for this problem [21].

The second flow we study consists of a turbulent boundary layer. Given the recent interpretation of the resolvent operator, where the nonlinear terms of the Navier-Stokes equations are modeled as a forcing term to an otherwise linear operator [2]; this has led the resolvent formalism to be extensively used in the study of turbulent flows, permitting insight into the present coherent structures. The current method allows the use of much larger domains in the streamwise and wall-normal direction in a computationally efficient manner and therefore it is of interest to the turbulence community.

The paper is organized as follows: Section II reviews the method for global resolvent calculations and introduces the parabolic approach along with the optimization procedure for the computation of suboptimals; in Sec. III the evaluated base flows are outlined; Sec. IV presents a comparison of the computational cost of the method to the global calculation; the studies of the Falkner-Skan and turbulent boundary layer are performed in Secs. V and VI; and conclusions are drawn in Sec. VII.

II. METHODS FOR COMPUTATION OF RESOLVENT MODES

A. Global resolvent modes

Here, we first describe the classical method for computation of resolvent modes. One starts by considering the forced linearized Navier-Stokes equations. A Fourier decomposition of the forcing and response is performed in terms of waves with a real frequency ω and a real spanwise wave number β,

$$\mathbf{F}(x, y, z, t) = \hat{\mathbf{F}}(x, y, \omega, \beta)e^{i(\beta z-\omega t)}, \tag{1}$$

$$\mathbf{q}(x, y, z, t) = \hat{\mathbf{q}}(x, y, \omega, \beta)e^{i(\beta z-\omega t)}, \tag{2}$$

where $\mathbf{q}(x, y, z, t)$ corresponds to the three velocity components and pressure. Substitution of the ansatz (1) and (2) in the linearized incompressible Navier-Stokes equations permits an arrangement in the form of an input-output system relating forcing terms and associated flow responses,

$$(-i\omega\mathbf{I} - \mathbf{G})\hat{\mathbf{q}} = \mathcal{P}\hat{\mathbf{F}}, \tag{3}$$

$$\hat{\mathbf{u}} = \mathcal{H}\hat{\mathbf{q}}. \tag{4}$$

Operator $\mathbf{G}$ denotes the Navier-Stokes equations linearized around a base flow and $\hat{\mathbf{u}} = (\hat{u} \;\; \hat{v} \;\; \hat{w})^T$; matrix $\mathcal{P}$ ensures that no forcing is applied to the continuity equation and matrix $\mathcal{H}$ is used to select the velocity components from the state $\hat{\mathbf{q}}$. The resolvent operator is then defined as

$$\mathcal{R} = \mathcal{H}{\mathcal{L}_{\mathbf{RES}}}^{-1}\mathcal{P} \tag{5}$$

where $\mathcal{L}_{\mathbf{RES}} = (-i\omega\mathbf{I} - \mathbf{G})$, such that

$$\hat{\mathbf{u}} = \mathcal{R}\hat{\mathbf{F}}. \tag{6}$$

The objective is to maximize the norm of the response with a forcing of minimum norm. This can be accomplished via the adjoint resolvent operator through an eigenvalue problem,

$$\mathcal{R}^*\mathcal{R}\hat{\mathbf{F}} = \sigma^2\hat{\mathbf{F}}, \tag{7}$$

where $\mathcal{R}^* = \mathcal{H}^*(\mathcal{L}_{\mathbf{RES}}{}^*)^{-1}\mathcal{P}^*$ is the adjoint resolvent operator.

In this work, Eq. (7) is solved via an iterative method; operators $\mathcal{L}_{\mathbf{RES}}$ and $\mathcal{L}_{\mathbf{RES}}{}^*$ are constructed using sparse matrices with the streamwise and wall-normal derivatives obtained from finite differences and Chebyshev polynomials, respectively. The sparse matrices allow the use of a lower-upper (LU) decomposition, which reduces memory requirements, such that the inverses $\mathcal{L}_{\mathbf{RES}}$ and $\mathcal{L}_{\mathbf{RES}}{}^*$ are not computed. For further details regarding the global resolvent calculation, the reader is referred to Refs. [20,39].

B. Parabolic resolvent computation method

In this section, we describe our approach to compute resolvent modes which is based on the linearized boundary-layer equations. We consider the general case where viscosity is dependent on the wall-normal and streamwise coordinates [47–50], which is of particular importance for application in turbulent flows. For this case, the nondimensional continuity and Navier-Stokes equations linearized around a two-dimensional base-flow, $\mathbf{U}(x, y) = [U(x, y)\ V(x, y)\ 0]^T$, are written as

$$\frac{\partial u}{\partial x} + \frac{\partial v}{\partial y} = 0, \tag{8}$$

$$\frac{\partial \mathbf{u}}{\partial t} + \nabla\mathbf{u}\cdot\mathbf{U} + \nabla\mathbf{U}\cdot\mathbf{u} = -\nabla p + \nabla\cdot[\nu_T(\nabla\mathbf{u} + \nabla\mathbf{u}^T)], \tag{9}$$

where $\mathbf{u} = (u\ v\ w)^T$ corresponds to the velocity fluctuations, which are nondimensionalized using the free-stream velocity, U_∞, and $\nu_T = (1 + \nu_t)/Re$ is the total nondimensional viscosity corresponding to the sum of the molecular and eddy viscosity contributions. The Reynolds number is defined as $\mathrm{Re} = U_\infty\delta_0^*/\nu^*$ with δ_0^* corresponding to the displacement thickness on the beginning of the computational domain and ν^* corresponding to the dimensional molecular viscosity; the flow is periodic along the spanwise direction.

The application of an eddy viscosity model for a turbulent flow follows from Ref. [51], in order to model the action of incoherent fluctuations on coherent structures. As a simplification, the eddy viscosity model has been commonly applied for all the scales, as reviewed in Ref. [2]. In the context of the resolvent method, where the nonlinear terms of the Navier-Stokes equations are treated as an unknown forcing to an otherwise linear operator, one approach consists in modeling part of the nonlinear forcing with an eddy viscosity, modifying the linear operator, as in Refs. [1,47,48]. This approach has obtained success in the literature, reproducing some of the trends observed in turbulent flows, such as the double peak in the premultiplied spectrum [47]; however, other trends are not reproduced, such as the peak phase speed [52]. The actual structure of the nonlinear forcing has been recently computed [18] where the eddy viscosity model has been observed to mimic it under certain conditions. In the current work, the use of an eddy viscosity model is made to keep the generality of the approach for the case of a wall-normal dependent viscosity. Different approaches could be considered, such as using only the turbulent mean, with a constant molecular viscosity, as in Refs. [3,4].

In this work, we focus on algebraically growing disturbances, such is the case for streaky structures in laminar and turbulent boundary layers, which are the most amplified fluctuations in these cases [29,47]. The problem is written in the frequency-wave number (ω, β) domain, where solutions are assumed to take the ansatz

$$\mathbf{q}(x, y, z, t) = \hat{\mathbf{q}}(x, y, \omega, \beta)\exp[i\beta z - i\omega t], \tag{10}$$

where the resulting stability equations are used to determine the spatial evolution of three-dimensional, time-dependent disturbances $\mathbf{q} = (u,\ v,\ w,\ p)^T$, corresponding to velocity and

pressure fluctuations. The streamwise variation is captured in the amplitude function $\hat{\mathbf{q}}$ alone and we are restricted to low frequencies ($\omega \ll 1$). Introduction of the ansatz of Eq. (10) in the linearized boundary-layer equations leads to the parabolic boundary layer equations [28–30], which can be written in matrix form as

$$\mathcal{A}\hat{\mathbf{q}} + \mathcal{B}\frac{\partial \hat{\mathbf{q}}}{\partial y} + \mathcal{C}\frac{\partial^2 \hat{\mathbf{q}}}{\partial y^2} + \mathcal{D}\frac{\partial \hat{\mathbf{q}}}{\partial x} = 0. \tag{11}$$

It should be noted that Eq. (11) is exactly parabolic such that application of a spatial marching is straightforward. Nevertheless, this equation is not valid for wavy disturbances, where the spatial wave number is nonzero. For such case, an auxiliary condition would be necessary, as in the parabolized stability equations [46,53,54]. The operators in (11) are given as

$$\mathcal{A} = \begin{pmatrix} 0 & 0 & i\beta & 0 \\ -i\omega + \beta^2 \nu_T + dU/dx & dU/dy & 0 & 0 \\ dV/dx & -i\omega + \beta^2 \nu_T + dV/dy & 0 & 0 \\ 0 & i\beta \partial \nu_T/\partial y & -i\omega + \beta^2 \nu_T & i\beta \end{pmatrix}, \tag{12}$$

$$\mathcal{B} = \begin{pmatrix} 0 & I & 0 & 0 \\ V + \partial \nu_T/\partial y & 0 & 0 & 0 \\ 0 & V + 2\partial \nu_T/\partial y & 0 & I \\ 0 & 0 & V + \partial \nu_T/\partial y & I \end{pmatrix}, \tag{13}$$

$$\mathcal{C} = \begin{pmatrix} 0 & 0 & 0 & 0 \\ -\nu_T & 0 & 0 & 0 \\ 0 & -\nu_T & 0 & 0 \\ 0 & 0 & -\nu_T & 0 \end{pmatrix}, \tag{14}$$

$$\mathcal{D} = \begin{pmatrix} I & 0 & 0 & 0 \\ U & \partial \nu_T/\partial y & 0 & 0 \\ 0 & U & 0 & 0 \\ 0 & 0 & U & 0 \end{pmatrix}, \tag{15}$$

where I is the identity matrix. The eddy viscosity acts as a wall-normal dependent Reynolds number; for $\nu_t = 0$, $\nu_T = \mathrm{Re}^{-1}$ and the usual operators are recovered, as in Ref. [29], for example.

Equation (11) is integrated in the streamwise direction using a first-order explicit Euler method. Discretization along the wall-normal direction is performed by means of Chebyshev polynomials. Dirichlet boundary conditions are applied for the three velocity components on the wall and at the maximum wall-normal location, $y_{\max}$.

The current approximation does not allow the study of problems with high values of ω, as in such cases the perturbation will have rapid variation in x which is not compatible with the boundary-layer approximations. Such cases could be relevant for aeroacoustics problems (as in Ref. [13]) or for the study of the interaction between oblique waves associated to nonlinear receptivity [55,56], for example. Nevertheless, $\omega = 0$ fluctuations are the most amplified and have been mostly studied in the literature. In the work of Ref. [30], it is shown that for the frequency region where streaky structures occur in boundary layers, parabolic calculations are within their range of validity. Nevertheless, the amplifications with respect to varying frequency are evaluated in Sec. V, for a Falkner-Skan boundary layer profile, confirming this assumption.

C. The global optimization problem

A forcing term, which could also model the nonlinear terms of the NS equations, $\hat{\mathbf{F}} = (0\ f_x\ f_y\ f_z)^T$, is introduced in the boundary layer equations (11), and these are written in a compact form as

$$\mathcal{L}\hat{\mathbf{q}} = \hat{\mathbf{F}}, \tag{16}$$

where the spatial, frequency, and wave-number dependencies have been absorbed into operator $\mathcal{L}$ as

$$\mathcal{L} = \mathcal{A} + \mathcal{B}D_y + \mathcal{C}D_y^2 + \mathcal{D}D_x, \tag{17}$$

where D_y and D_x are derivative operators along the wall-normal and streamwise directions.

We proceed by defining the inner product between two square integrable vector functions, $\Psi(x, y) = [\psi_1(x, y) \quad \psi_2(x, y) \quad \psi_3(x, y) \quad \psi_4(x, y)]^T$ and $\Phi(x, y) = [\phi_1(x, y) \quad \phi_2(x, y) \quad \phi_3(x, y) \quad \phi_4(x, y)]^T$, as

$$\langle \Psi(x, y), \Phi(x, y) \rangle = \int_{x_0}^{x_f} \int_0^{\infty} \overline{\Psi}(x, y)\Phi(x, y) dy dx, \tag{18}$$

where the overline corresponds to the conjugate transpose, and x_0 and x_f account for the streamwise domain. Discretization of Eq. (18) reads

$$\langle \mathbf{\Psi}, \mathbf{\Phi} \rangle = \mathbf{\Psi}^H \mathcal{W} \mathbf{\Phi}, \tag{19}$$

where the superscript H corresponds to the Hermitian and $\mathcal{W}$ accounts for the integration of the four components along the wall-normal and streamwise directions which correspond to a Chebyshev and a Cartesian grid, respectively.

The kinetic energy of the fluctuations $\hat{\mathbf{q}} = (\hat{u}\ \hat{v}\ \hat{w}\ \hat{p})^T$ is then computed from

$$\langle \hat{\mathbf{q}}, \hat{\mathbf{q}} \rangle_q = \hat{\mathbf{q}}^H \mathcal{W} \mathcal{M}_q \hat{\mathbf{q}}, \tag{20}$$

where matrix $\mathcal{M}_q$ defines a measure of the disturbance and accounts only for the velocity fluctuations inside the boundary layer, an approach which allows avoiding unphysical results for very low values of β (see Ref. [33]).

Similarly, the norm for the forcing is obtained from

$$\langle \hat{\mathbf{F}}, \hat{\mathbf{F}} \rangle_f = \hat{\mathbf{F}}_1^H \mathcal{W} \mathcal{M}_f \hat{\mathbf{F}}_2, \tag{21}$$

where $\mathcal{M}_f$ ensures that only the momentum equations are forced, and the forcing here is allowed to extend throughout the wall-normal direction. Nevertheless, restrictions regarding the spatial support of the forcing may also be imposed via modifications of operator $\mathcal{M}_f$.

The figure of merit for the optimization is taken as the total kinetic energy gain of the perturbations inside the domain per unit of forcing, as

$$G = \frac{\langle \hat{\mathbf{q}}, \hat{\mathbf{q}} \rangle_q}{\langle \hat{\mathbf{F}}, \hat{\mathbf{F}} \rangle_f}, \tag{22}$$

maximizing the gain in Eq. (22) is equivalent to maximizing the fluctuation energy subject to unit forcing norm, i.e., $\langle \hat{\mathbf{F}}, \hat{\mathbf{F}} \rangle_f = 1$.

By maximizing Eq. (22), resolvent modes for algebraically growing disturbances are readily obtained. The constrained maximization of the cost function, where the constraint is given by the forced parabolic boundary layer equations (16), is solved by transforming the problem into a nonconstrained optimization by means of Lagrange multipliers [57] and searching for stationary points. We define an augmented functional as

$$J = G - \mathrm{Re}(\langle \hat{\mathbf{q}}^*, \mathcal{L}\hat{\mathbf{q}} - \hat{\mathbf{F}} \rangle), \tag{23}$$

where $\hat{\mathbf{q}}^*$, the Lagrange multiplier, is referred to as the adjoint variable.

Taking the variation of Eq. (23), one reaches

$$\delta J = \langle \hat{\mathbf{q}}, \delta\hat{\mathbf{q}} \rangle_q - \Re(\langle \hat{\mathbf{q}}^*, \mathcal{L}\delta\hat{\mathbf{q}} - \delta\hat{\mathbf{F}} \rangle - \langle \delta\hat{\mathbf{q}}^*, \mathcal{L}\hat{\mathbf{q}} - \hat{\mathbf{F}} \rangle), \tag{24}$$

where δJ corresponds to the sensitivity of the Lagrangian functional to infinitesimal changes, $\delta\hat{\mathbf{q}}$, $\delta\hat{\mathbf{F}}$, and $\delta\hat{\mathbf{q}}^*$. When the variation becomes zero, this corresponds to a stationary point. The third term, $\langle \delta\hat{\mathbf{q}}^*, \mathcal{L}\hat{\mathbf{q}} - \hat{\mathbf{F}} \rangle$, is equal to zero, if $\hat{\mathbf{q}}$ is a solution of the state equation, given that it corresponds to

the inner product between the adjoint and the state equation. Setting the second term to zero results in the adjoint problem with corresponding boundary and initial conditions. This is derived in what follows.

The operators are moved to the left side of the inner product by considering the definition of the adjoint,

$$\langle \hat{\mathbf{q}}^*, \mathcal{A}\hat{\mathbf{q}} \rangle = \langle \mathcal{A}^*\hat{\mathbf{q}}^*, \hat{\mathbf{q}} \rangle, \tag{25}$$

where the star $*$ denotes the adjoint. For matrix operators, the adjoint becomes simply a conjugate transpose, or Hermitian. The derivatives are moved from the direct to the adjoint variable by integrations by parts, leading to

$$\delta J = \langle \hat{\mathbf{q}}, \delta\hat{\mathbf{q}} \rangle_q - \mathrm{Re}(\langle (\mathcal{A}^* - \mathcal{B}_y^* - \mathcal{D}_x^*)\hat{\mathbf{q}}^* - \mathcal{B}^*\hat{\mathbf{q}}_y^* + \mathcal{C}^*\hat{\mathbf{q}}_{yy}^* - \mathcal{D}^*\hat{\mathbf{q}}_x^*, \delta\hat{\mathbf{q}} \rangle + \langle \hat{\mathbf{q}}^*, \delta\hat{\mathbf{F}} \rangle) + \text{b.c.} \tag{26}$$

The first and second terms are combined in order to define the adjoint equations for this particular optimization, which is forced by the direct solution,

$$\mathcal{L}^*\hat{\mathbf{q}}^* = (\mathcal{A}^* - \mathcal{B}_y^* - \mathcal{D}_x^*)\hat{\mathbf{q}}^* - \mathcal{B}^*\hat{\mathbf{q}}_y^* + \mathcal{C}^*\hat{\mathbf{q}}_{yy}^* - \mathcal{D}^*\hat{\mathbf{q}}_x^* = \mathcal{M}_q\hat{\mathbf{q}}. \tag{27}$$

The term b.c. in (26) corresponds to four integrals which, once set to zero, supply the boundary and initial conditions for the adjoint boundary layer equations, leading to

$$\int_{x_0}^{x_f} \langle \mathcal{B}^*\hat{\mathbf{q}}^*, \delta\hat{\mathbf{q}} \rangle|_0^{y_{\max}} dx = \int_{x_0}^{x_f} (V\overline{\hat{u}}^*\delta\hat{u} + (\overline{\hat{p}}^* + V\overline{\hat{v}}^*)\delta\hat{v} + V\overline{\hat{w}}^*\delta\hat{w} + \overline{\hat{v}}^*\delta\hat{p})|_0^{y_{\max}} dx = 0, \tag{28}$$

$$\int_{x_0}^{x_f} \langle \mathcal{C}^*\hat{\mathbf{q}}^*, \delta\hat{\mathbf{q}}_y \rangle|_0^{y_{\max}} dx = \int_{x_0}^{x_f} (-\overline{\hat{u}}^*\delta\hat{u}_y - \overline{\hat{v}}^*\delta\hat{v}_y - \overline{\hat{w}}^*\delta\hat{w}_y)|_0^{y_{\max}} dx = 0, \tag{29}$$

$$\int_{x_0}^{x_f} \langle \mathcal{C}^*\hat{\mathbf{q}}_y^*, \delta\hat{\mathbf{q}} \rangle|_0^{y_{\max}} dx = \int_{x_0}^{x_f} (-\overline{\hat{u}}_y^*\delta\hat{u} - \overline{\hat{v}}_y^*\delta\hat{v} - \overline{\hat{w}}_y^*\delta\hat{w})|_0^{y_{\max}} dx = 0, \tag{30}$$

$$\int_0^{\infty} ((\overline{\hat{p}}^* + U\overline{\hat{u}}^*)\delta\hat{u} + U\overline{\hat{v}}^*\delta\hat{v} + U\overline{\hat{w}}^*\delta\hat{w})|_{x_0}^{x_f} dy = 0, \tag{31}$$

where $y_{\max}$ corresponds to the maximum wall-normal location being considered.

Therefore, for this particular optimization, the boundary and terminal conditions for the adjoint velocities are set to zero,

$$\overline{\hat{u}}^* = \overline{\hat{v}}^* = \overline{\hat{w}}^*|_{y=0} = 0, \tag{32}$$

$$\overline{\hat{u}}^* = \overline{\hat{v}}^* = \overline{\hat{w}}^*|_{y=y_{\max}} = 0, \tag{33}$$

and

$$\hat{u}^*(x = x_f) = \hat{v}^*(x = x_f) = \hat{w}^*(x = x_f) = 0. \tag{34}$$

Finally, Eq. (26), which corresponds to the variation of the cost functional, reduces to an inner product between the adjoint and the variation of the forcing term, which can be written as

$$\delta J = \langle \hat{q}^*, \delta\hat{\mathbf{F}} \rangle = \int_{x_0}^{x_f} \int_0^{\infty} \overline{\hat{q}^*}(x, y)\delta\hat{\mathbf{F}} dy dx. \tag{35}$$

The term δJ may be also computed using the definition of the directional derivative, on this case, of $\delta\hat{\mathbf{F}}$ along the gradient of J,

$$\delta J = \langle \overline{\nabla}_{\mathbf{F}} J, \delta\hat{\mathbf{F}} \rangle = \int_{x_0}^{x_f} \int_0^{\infty} \overline{\nabla}_{\mathbf{F}} J \delta\hat{\mathbf{F}} dy dx, \tag{36}$$

where $\overline{\nabla}_{\mathbf{F}} J$ is the gradient of the functional with respect to the forcing. From Eqs. (35) and (36) we find that this gradient is equal to the adjoint variable,

$$\nabla_{\mathbf{F}} J = \hat{\mathbf{q}}^*. \tag{37}$$

Since the term $\mathcal{L}\hat{\mathbf{q}} - \hat{\mathbf{F}}$ in Eq. (23) is equal to zero, the gradient of J with respect to the forcing corresponds to the gradient of the total energy gain with respect to the forcing. This is a standard procedure in adjoint optimization methods and the reader is referred to Ref. [57] for further details concerning its derivation.

Once the gradient is available, the steepest descent method can be used to compute the optimal forcing and resulting modes, which are equivalent to the dominant resolvent modes for $\alpha = 0$,

$$\hat{\mathbf{F}}_{n+1} = \hat{\mathbf{F}}_n + \gamma \nabla_{\mathbf{F}} J \delta \hat{\mathbf{F}}_n, \tag{38}$$

where γ is a parameter that defines how much of the gradient is used to compute the updated value of the forcing. The method described here is a modification of the procedure introduced in Ref. [31] for the computation of actuation shapes for closed-loop flow control and can be summarized in the following algorithm:

(1) Start with a random force field and null initial conditions and integrate the direct problem up to the desired position.

(2) The solution of the direct problem is used to force the adjoint equations, which are solved from the final to the initial position, with null terminal conditions.

(3) The resulting adjoint field corresponds to the gradient of the cost function with respect to the forcing and can then be used to update the forcing towards its optimal value.

(4) With the new force field, start from the first step and continue up to convergence of the total energy.

D. Suboptimal modes using Krylov-Arnoldi

The method described in the previous section is quite efficient computationally and in general rapidly converges to the dominant resolvent modes. It corresponds to a power iteration method to obtain the leading resolvent mode [38,39]. However, its drawback lies in the fact that only the first mode can be computed, with the suboptimal modes and eigenvalues not available. These can be computed by means of the Krylov-Arnoldi decomposition [35,39]. A more thorough description of this method can be also found in Ref. [58].

The direct-adjoint iterations converge to the leading mode with an error which is associated to the eigenvalue separation, reducing by a factor of $(\lambda_1/\lambda_2)^2$ after each iteration, where λ_n are the nth order eigenvalues [39]. Alternatively, eigenvalues can be estimated based on a subspace spanned by a sequence of vectors $\hat{f}_n$, based on Krylov-Arnoldi iterations, which is briefly summarized here.

It can be shown that singular values and singular vectors of the resolvent operator, $\mathcal{L}$, can be obtained from an eigenvalue decomposition of $\mathcal{L}^*\mathcal{L}$ [35,39]. We therefore seek for a low-rank representation of $\mathcal{L}^*\mathcal{L}$. We start by defining matrices $\mathbf{F}_s = [\hat{f}_1, \hat{f}_2, \ldots, \hat{f}_n]$, corresponding to a Krylov subspace, and $\mathbf{W}_s = [\hat{w}_1, \hat{w}_2, \ldots, \hat{w}_n] = [\mathcal{L}^*\mathcal{L}\hat{f}_1 \mathcal{L}^*\mathcal{L}\hat{f}_2 ... \mathcal{L}^*\mathcal{L}\hat{f}_n]$. The elements of $\mathbf{W}_s$ thus correspond to the adjoint fields obtained from one direct and one adjoint computation. As for the forcing matrix $\mathbf{F}_s$, its elements are obtained by means of the Arnoldi algorithm, the elements $\hat{f}_n$ consist in using $\hat{w}_{n-1}$ made orthonormal to all previous $\hat{f}_{n-1}$. This is obtained by means of a Gram-Schmidt orthonormalization,

$$\hat{f}_n = \hat{w}_{n-1} - F_{0,\ldots,n-1}\hat{\theta} \tag{39}$$

with

$$F_{0,\ldots,n-1} = [\hat{f}_1, \hat{f}_2, \ldots, \hat{f}_{n-1}] \tag{40}$$

and

$$\hat{\theta}_i = \left(F^H_{0,\ldots,n-1} W_{\text{cheb}} F^*_{0,\ldots,n-1} W_{\text{cheb}} \hat{w}_{n-1}\right). \tag{41}$$

By construction,

$$\mathcal{L}^*\mathcal{L}\hat{f}_n = \hat{w}_n \tag{42}$$

such that

$$\mathcal{L}^*\mathcal{L}\mathbf{F}_s = \mathbf{W}_s. \tag{43}$$

A QR decomposition is then performed on $\mathbf{F}_s$,

$$\mathbf{F}_s = \mathbf{QR} \tag{44}$$

with $\mathbf{Q}$ a unitary matrix and $\mathbf{R}$ upper triangular. Matrix $\mathbf{H}_f$ is defined as

$$\mathbf{H}_f = \mathbf{Q}^*\mathbf{R}^{-1} \tag{45}$$

and eigenvalues and vectors of $\mathcal{L}^*\mathcal{L}$ within the Krylov subspace are obtained from an eigendecomposition of $\mathbf{H}_f$,

$$\mathbf{H}_f\Psi = \Gamma^2\Psi. \tag{46}$$

Forcing modes are then obtained from

$$V_i = \mathbf{Q}\Psi \tag{47}$$

with the corresponding response modes obtained from a solution of the direct equations with the corresponding suboptimal forcing. In summary, the Krylov-Arnoldi method can be combined with the direct-adjoint iterations from the previous section, leading to a computational efficient way of computing parabolic resolvent optimal and suboptimal modes. The algorithm is outlined as follows:

(1) Start with a random force field that defined the first column of $\mathbf{F_s}$.

(2) The direct problem is solved using the forcing f_n at the corresponding nth and null initial conditions to integrate the direct equations from x_0 to x_f.

(3) The solution is used to force the adjoint equation, which is integrated from x_f to x_0, with null terminal conditions.

(4) The corresponding column of $\mathbf{W_s}$ is given by $\hat{q}_n^*$, nth solution of the adjoint equation.

(5) The subsequent column of matrix $\mathbf{F}_s$ is given by w_n, normalized with respect to the previous column, using Eqs. (39)–(41). This is used as a forcing for the direct equations, continuing the method from (2).

The algorithm is performed for a sufficient number of iterations in order to ensure that the suboptimal modes will be converged. Suboptimal forcings and eigenvalues are then obtained from (44) to (47), with the corresponding suboptimal modes obtained from the solution of the direct equations for each of the forcings considered.

III. EVALUATED BASE FLOWS

A. Falkner-Skan boundary layer

Some of the base flows considered here belong to the Falkner-Skan family of the boundary layer flows, including cases with both adverse and favorable streamwise pressure gradients. The free stream streamwise velocity obeys a power law, $U_\infty(x) = Cx^m$, and the spanwise component of it is null, $W_\infty = 0$. We introduce the similarity parameter

$$\eta(x^d, y^d) = \sqrt{\frac{m+1}{2}}\sqrt{\frac{U_\infty}{\nu x^d}}\, y^d \tag{48}$$

and the stream function

$$\Psi^d = \sqrt{\frac{2}{m+1}}\sqrt{U_\infty \nu x^d}\, f(\eta), \tag{49}$$

with the dimensional velocities $U^d = \partial\Psi^d/\partial y^d$ and $V^d = -\partial\Psi^d/\partial x^d$. Here, the superscript d denotes dimensional values. The boundary layer profiles are then derived from the solution of the

nonlinear differential equation (see, e.g., Ref. [59])

$$f''' + ff'' + \beta_H(1 - f'^2) = 0, \tag{50}$$

where

$$\beta_H = \frac{2m}{m+1}. \tag{51}$$

This equation is subjected to the boundary conditions given by $f = f' = 0$, at $\eta = 0$ and $f' \to 1$ when $\eta \to \infty$. Equation (50) may be solved via a shooting method. The resulting velocity profiles in the streamwise and wall-normal directions are then given as

$$U^d(x, y) = f'(\eta)U_\infty(x), \tag{52}$$

$$V^d(x, y) = -\sqrt{\frac{m+1}{2}}\sqrt{\frac{\nu}{U_\infty x}}\left[f + \frac{m-1}{m+1}\eta f'\right]U_\infty(x). \tag{53}$$

The displacement thickness can then be computed as

$$\delta^* = \left[\int_0^\infty (1 - f')d\eta\right][(m+1)U_\infty/2\nu x^d]^{-1/2}, \tag{54}$$

which implies that its value in the beginning of the domain is given as

$$\delta_0^* = \left[\int_0^\infty (1 - f')d\eta\right]\left[(m+1)U_0/2\nu x_0^d\right]^{-1/2}, \tag{55}$$

such that x_0^d is a fixed position where the streamwise velocity is U_0 and the corresponding Reynolds number is Re. The value of η in terms of the nondimensional coordinates is then

$$\eta(x, y) = \left[\int_0^\infty (1 - f')d\eta\right]\left[\frac{U_\infty}{U_0 x}\right]^{1/2} y, \tag{56}$$

where the spatial nondimensional coordinates are x, y, and z, for the streamwise, wall-normal and spanwise directions which, in this work, consider the displacement thickness in the beginning of the computational domain (δ_0^*) in their nondimensionalization.

B. Turbulent boundary layer

The second base flow for the application of the parabolic resolvent calculation consists of a turbulent boundary layer with a variable eddy viscosity. The self consistent expression proposed by Ref. [60] is considered and a corresponding variable eddy viscosity is computed following the approach described in Ref. [47]. The mean flow is given as

$$U = u_\tau[U_i^+(y^+) - U_{\log}^+(y^+) + U_e^+(\mathrm{Re}) - U_w^+(\mu)], \tag{57}$$

where u_τ is the wall friction velocity, $\mu = y/\Delta$ where Δ is the Rotta-Clauser outer length scale, $\Delta = \delta^*/U_e^+$, and the $+$ superscript indicates quantities which are nondimensionalized using inner variables (i.e., $l = \nu/u_\tau$ and u_τ, the characteristic length and velocity); as for the laminar case, the Reynolds number is defined in terms of the free stream velocity, displacement thickness and molecular viscosity. The explicit expressions for the free-stream (U_e^+), inner layer (U_i^+), log layer ($U_{\log}^+$), and wake function (U_w^+) velocities may be found in Ref. [47] and are included in the Appendix A, for completeness. Quantities which are presented without the $+$ superscript are nondimensionalized with the outer scales which, in this case, correspond to the displacement thickness and the free-stream velocity. The characteristic velocities and lengths both for the inner and outer scales are considered in the beginning of the computational domain.

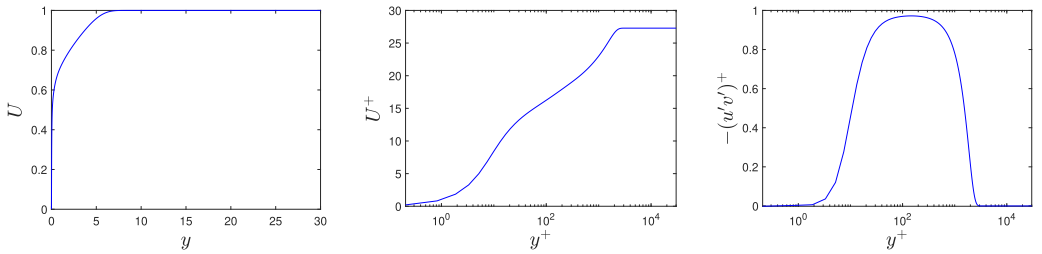

FIG. 1. Mean velocity scaled in outer (a) and inner (b) units and corresponding Reynolds stresses in inner units (c) for Re = 10 000.

The total viscosity is related to the total shear stress as

$$\frac{\tau}{\rho} = \nu_T(y)\frac{\partial U}{\partial y}. \tag{58}$$

The total shear stress may also be computed by integrating the mean momentum equation in the wall-normal direction,

$$\frac{\tau}{\rho} = u_\tau^2 + \int_0^y \left(U\frac{\partial U}{\partial x} + V\frac{\partial U}{\partial y}\right)dy, \tag{59}$$

where the wall-normal component may be obtained from the continuity equation,

$$V = -\int_0^y \left(\frac{\partial U}{\partial x}\right)dy. \tag{60}$$

Finally, the term $\partial U/\partial x$ is obtained by deriving Eq. (57) with respect to x. The total viscosity can then be computed from (58) and (59). The scaling of the streamwise domain has also been proposed in Ref. [60] and is included in the Appendix. For further details concerning this procedure, the reader is referred to Ref. [47].

In order to illustrate the results, Fig. 1 presents the mean flow for Re = 10 000 along with the Reynolds stress scaled in inner units, which can be computed from

$$\frac{-\langle u'v'\rangle}{u_\tau^2} = \frac{\tau/\rho - \nu\frac{\partial U}{\partial y}}{u_\tau^2}. \tag{61}$$

Similarly to the laminar flow case, for the turbulent boundary layer profile we consider the inlet velocity and displacement thickness as reference quantities for the computation of the resolvent modes.

IV. VALIDATION AND COMPUTATIONAL COST

In this section, the parabolic resolvent method is compared to the more usual approach to compute resolvent modes, which is based in matrix calculations.

A. Computational cost and comparison to the parabolic resolvent

Performing the singular value decomposition (SVD) in a locally parallel problem is straightforward and results may be found in the literature for a wide range of geometries (see, for example, Refs. [12,13,33]. The wall-normal direction is discretized with a Chebyshev grid, such that matrix $\mathcal{R}$ is $[4n_y \times 4n_y]$, for the three velocity components and pressure, with n_y Chebyshev points. The resulting size of the problem permits a direct computation of the SVD.

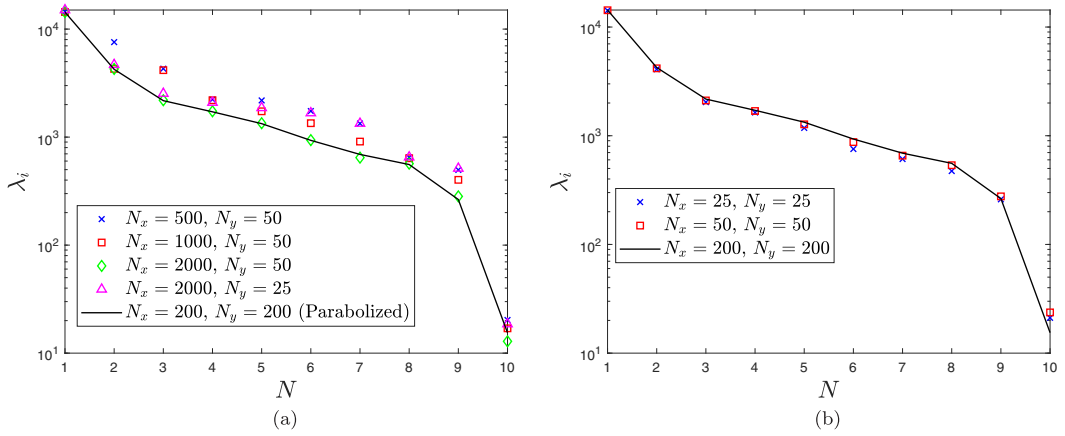

FIG. 2. Comparison between eigenvalues for different $n_x \times n_y$ combinations for (a) global and (b) parabolic calculations, where N is the mode number. The case with $n_x \times n_y = 200 \times 200$, for the parabolic calculation is plotted in both figures as a reference case.

On the other hand, for the global resolvent problem, $\mathcal{R}$ is $[4n_y n_x \times 4n_y n_x]$, where n_x is the streamwise discretization (taken as finite differences, in this work). The extra dimension requires dedicated algorithms for the computation of the modes, such as the shift-and-invert Arnoldi algorithm [61]. The bottleneck of the problem is the inversion of matrix $\mathcal{K} = (i\omega\mathcal{B} - \mathcal{A})$, which is explicitly made sparse and computed by means of the LU factorization. The overall cost of the solution corresponds to such factorization [35], which is of the order of $\approx N^3$, where $N = 4n_y n_x$. The use of finite differences for the streamwise derivatives and sparse matrices significantly decreases the computational expense; however, the memory requirements are still large, scaling with N^2. This trend causes the global computation to be intractable as the size of the domain increases, as is the case for nonparallel flows with large Reynolds numbers. For further details concerning the global resolvent computations, the reader is referred to Refs. [34,35].

For the parabolic resolvent approach, the streamwise direction is solved by means of a spatial marching (in this work taken as an explicit Euler method), which is computationally inexpensive. At each station, Eq. (16) is solved, which has the same computational cost as solving a locally parallel problem.

We now compare the results for a laminar (Falkner-Skan) boundary layer without the presence of a pressure gradient, i.e., a Blasius profile. The case considered extends from $\mathrm{Re}_0 = 300$ to $\mathrm{Re} = 1000$, for $(\omega, \beta) = (0, 0.1)$. The domain extends up to $y_{\max} = 60$ in the wall-normal direction. The characteristic length scale is considered as the displacement thickness in the beginning of the domain. Figure 2 presents the 10 first eigenvalues for different grid combinations, for the parabolic and global calculations. The case with $n_x \times n_y = 200 \times 200$, for the parabolic calculation is considered as a reference result, for this particular evaluation.

It is clear that the grid convergence is much more rapid for the parabolic calculation. If one considers the criterion of doubling the number of grid points with approximately unaltered results a requirement for convergence, we observe that the global calculation requires $n_x \times n_y = 2000 \times 50$ to converge the first two modes, whereas the same result is obtained with $n_x \times n_y = 50 \times 50$ for the parabolic case. The global resolvent calculation, for such grid, requires approximately 30 times more computational time and 2000 times more memory than the parabolic approach.

The velocity fluctuations for these two converged cases are compared in Fig. 3 at the end of the computational domain, where $\mathrm{Re} = 1000$. The behavior of the fluctuations in the $x - y$ is shown in Fig. 4. There is a compelling match between the two approaches both for the eigenvalues and shape of the resulting optimal fluctuations; a similar trend is also seen for the corresponding optimal

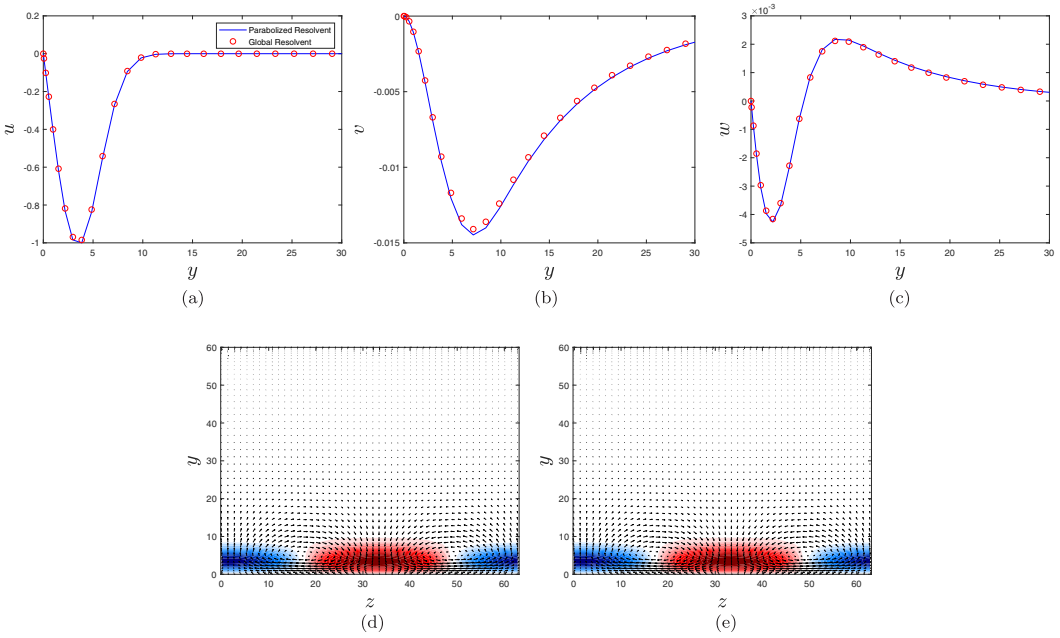

FIG. 3. Comparison between the envelope of the velocity fluctuations in panels (a)–(c) and behavior in the y-z plane in panels (d) [(e)] for the global [parabolic] resolvent for Re $= 1000$, $\beta = 0.1$, and $\omega = 0$ at the end of the computational domain. In panels (d) [(e)], the contour represents the streamwise velocity fluctuation and the arrows correspond to the velocity field composed of the spanwise [wall-normal] velocity fluctuations.

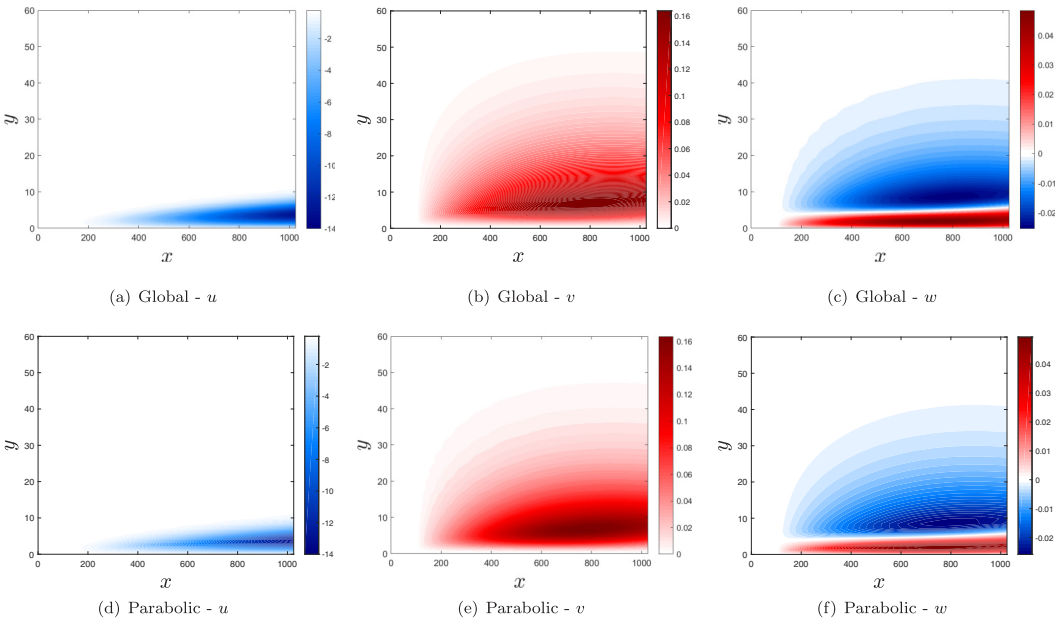

FIG. 4. Comparison between global [in panels (a)–(c)] and parabolic [in panels (d)–(f)] velocity fluctuations for u, v, and w in the x-y plane. The computation was performed for Re $= 1000$, $\beta = 0.1$, and $\omega = 0$, for a neutral pressure gradient

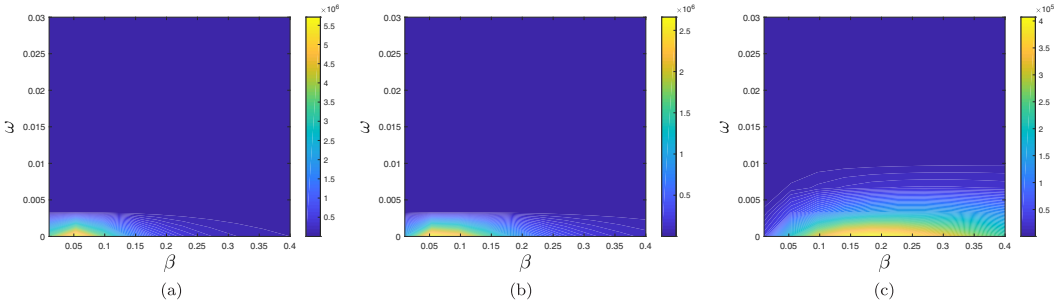

FIG. 5. Most amplified eigenvalue for Re = 5000 in the end of the computational domain and $m = -0.07$, 0.0, and 0.4 in panels (a)–(c), respectively. The color bar was adjusted for each plot in order to facilitate the evaluation of the results.

forcing, which is not shown for brevity. Although not shown for the sake of brevity, good agreement was also observed between the global and parabolic resolvent methods for the gains, forcing, and response for the other spanwise wave numbers and pressure gradients evaluated. The results display the usual behavior for the optimal fluctuations in a boundary layer: The optimal velocity fluctuations correspond to streaks and streamwise vortices, with the optimal mode presenting a strong dominance over the suboptimals.

V. RESOLVENT ANALYSIS OF FALKNER-SKAN BOUNDARY LAYERS

A. Reynolds β-ω dependencies

In this section, the behavior of the eigenvalues and modes, computed from the parabolic resolvent approach, is shown for the Falkner-Skan boundary layer mean profile. For all the cases, the Reynolds number at the start of the computational domain is equal to $\mathrm{Re}_0 = 300$. Figure 5 presents the behavior of the most amplified eigenvalue as a function of β and ω, for Re = 5000 at the end of the computational domain, for adverse, zero, and favorable pressure gradients, corresponding to $m = -0.07$, 0.0, and 0.4.

For all three cases, the most amplified mode occurs at $\omega = 0$, a feature which is also observed for the other Reynolds numbers and suboptimals evaluated. This behavior had already been observed in the literature for the optimal fluctuation, as shown in Ref. [29] for zero, in Ref. [41] for favorable or adverse pressure gradients, and in Ref. [38] for the optimal forcing case. Here we extend this result for the case of the optimal and suboptimal responses. It should also be noted that, for this case, the amplified frequencies are limited to $\omega \leqslant 0.02$, where the parabolic method is expected to be very accurate, as shown in Ref. [30]. If the frequency range were continuously increased, Tollmien-Schlichting waves would start to be amplified at a sufficiently high value of ω. For these high frequencies, which are out of the scope of the current work, the parabolic method would be inaccurate and a different approach would have to be used. From now on, only $\omega = 0$ fluctuations will be considered, as they are expected to dominate the dynamics of this flow. It should also be noted that the parabolic calculation is expected to be less accurate the higher the evaluated frequency, so the method is limited to small ω values.

A β-Re parametric study was performed for $\omega = 0$, with Re corresponding to the displacement-thickness-based Reynolds number at the end of the domain of interest, and the results are summarized in Fig. 6 for the most amplified eigenvalue, for adverse, zero, and favorable pressure gradients. For the three cases, the most amplified spanwise wave number, $\beta_{\max}$, is observed to be proportional to $1/\mathrm{Re}$ or, equivalently, $1/\sqrt{\mathrm{Re}_x}$, where $\mathrm{Re}_x = U_\infty x^d/\nu^d$, at the end of the computational domain. This feature had been observed in Ref. [28] for the optimal initial condition in

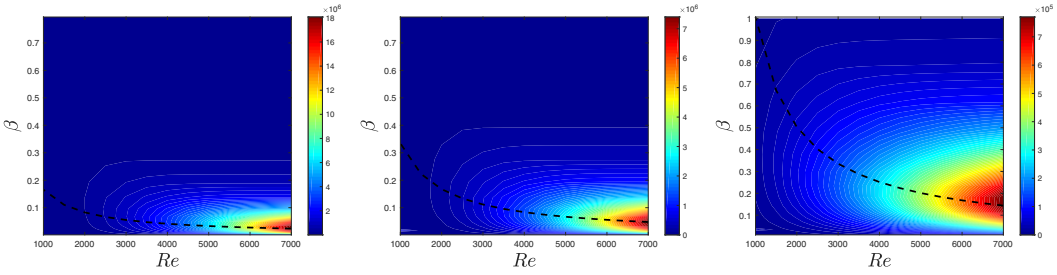

FIG. 6. Contour plots of the most amplified eigenvalue as a function of β-Re for adverse, zero, and favorable pressure gradients, respectively, for $\omega = 0$. The dashed curve represents the most amplified β for each Reynolds number. The color bar and vertical axis were adjusted for each plot in order to facilitate the evaluation of the results.

a zero-pressure gradient case and here is extended for the optimal forcing in favorable or adverse pressure gradient cases.

As expected, higher Reynolds numbers are associated with larger eigenvalue of the optimal fluctuation. Favorable and adverse pressure gradients have respectively a stabilizing and destabilizing effect. Increasing the Reynolds number has the added effect of leading to smaller β values for the optimal fluctuation, which is associated to larger structures in the wall-normal direction. This trend adds a computational difficulty as the wall-normal domain considered has to be larger to accommodate such structures which would further hinder the use of a global resolvent approach.

We now evaluate the effect of the Reynolds number on the gains for the case when the same streamwise separation is considered, which emulates the effect of a change in the streamwise velocity, U_∞, for the same physical domain. It can be shown that the nondimensional streamwise coordinate may be written as

$$\frac{x^d}{\delta_0^*} = \frac{x^d}{L}\frac{1}{c^2}\mathrm{Re}_0\frac{L}{x_0^d}, \tag{62}$$

where L is the physical length of the domain, x_0^d is the dimensional value where the optimization starts, and c is the displacement thickness written in terms of the Blasius length scale (see, e.g., Ref. [59]). By fixing L and x_0^d, the corresponding distance x^d/δ_0^* can be found for different Reynolds numbers. In this analysis, the domain where the optimization is performed extends from $x_0^d/L = 0.1$ up to $x^d/L = 1$ which, in no dimensional variables, corresponds to $1/c^2\mathrm{Re}_0 < x^d/\delta_0^* < 10/c^2 Re_0$. Figure 7 presents the most amplified gain for three sample Reynolds numbers, $\mathrm{Re}_0 = 1000$, 2000 and 3000 and the three pressure gradients considered in this study, $m = 0$, 0.4, and -0.07, normalized by Re_x^2 as a function of β, where Re_x is computed in the end of the computational domain. Where the energy gain, G, can be shown to be equivalent to λ_1^2. For the same pressure gradient, the curves for the different Reynolds number coalesce, indicating that the optimal gain scales with Re_x^2 or, equivalently, with Re^4, in the end of the computational domain. These results indicate that the effect of the optimal forcing in the laminar boundary layer is Reynolds independent, as previously observed [30]. Note that since the forcing and the velocity fluctuations have different dimensions, the numerical value of the gain, G, depends on the reference length and velocity, taken here as δ_0^* and U_0.

B. Shape of the most amplified modes and forcings

In this section, the modes and forcings for $\mathrm{Re} = 7000$ and the most amplified β are shown. As before, only the $\omega = 0$ case is considered, as it corresponds to the most unstable frequency; similar conclusions may be drawn for different Reynolds numbers. The three components of the optimal

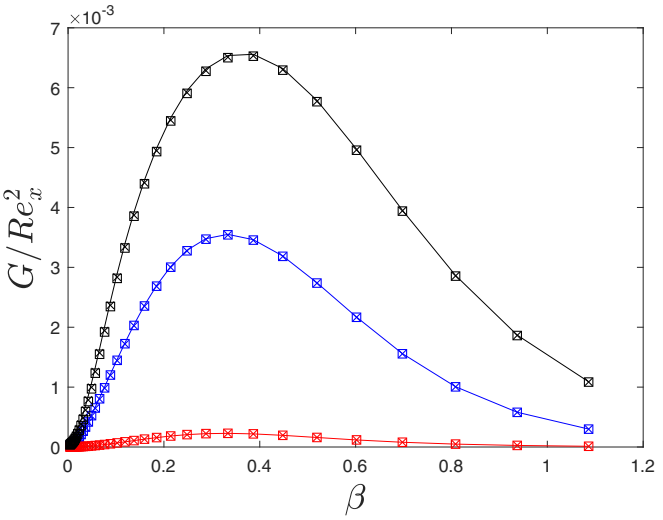

FIG. 7. Gains, G for the case of an adverse (black), zero (blue), and favorable (red) laminar boundary layer computed for three different Reynolds numbers, corresponding to $\mathrm{Re}_0 = 1000$, 2000, and 3000, in the beginning of the computational domain, in the solid line, circle, and cross symbols, respectively. Similar results have been observed independently of the Reynolds number considered. The gains have been normalized by Re_x^2.

forcing up to mode 3 are shown in Fig. 8 and the corresponding responses are given in Fig. 9, for the case of the zero pressure gradient. Similar observations can be made to the other pressure gradient cases, for their corresponding most amplified β. The dashed line in the plots highlights the boundary layer thickness. The envelope of the velocities and forces is given at $x = 27\,000$, in Fig. 10. The corresponding kinetic energy of the velocity fluctuations as a function of the streamwise direction is shown in Fig. 11.

The optimal and suboptimal responses are dominated by the streamwise component of the velocity fluctuation which is contained inside the boundary layer. The three first modes correspond to streaky structures with a different wall-normal support and streamwise behavior. The most amplified mode grows up to end of the domain, whereas the second and third modes saturate at a given streamwise component, at a moment when a second streaky structure appears. Such behavior is clear when evaluating the energy of the fluctuations in the streamwise direction, as presented in Fig. 11.

In all the cases, the wall-normal and spanwise components of the optimal force dominate its dynamics, in a mechanism which is related to lift-up [62]. It should also be noted that the forcing components extend outside of the boundary layer, within the free-stream region. Finally, unlike the optimal perturbation scenario, where the wall-normal and spanwise velocity components decay along the chord, for the optimal forcing case these components also grow along this direction, as they are continuously driven by forcing components. Both of these trends are relevant for the receptivity of free-stream turbulence. Similar trends can be observed for the other Reynolds numbers and pressure gradients evaluated.

C. Relevance for free-stream turbulence receptivity

Free-stream turbulence is among the most complicated scenarios for transition as both the boundary layer and the FST characteristics change in the downstream direction. The fluctuations grow algebraically inside the boundary layer due to the lift-up effect [63,64] given the non-normality of the Navier-Stoker operator [8,65]. Even though the resulting fluctuations are in good agreement

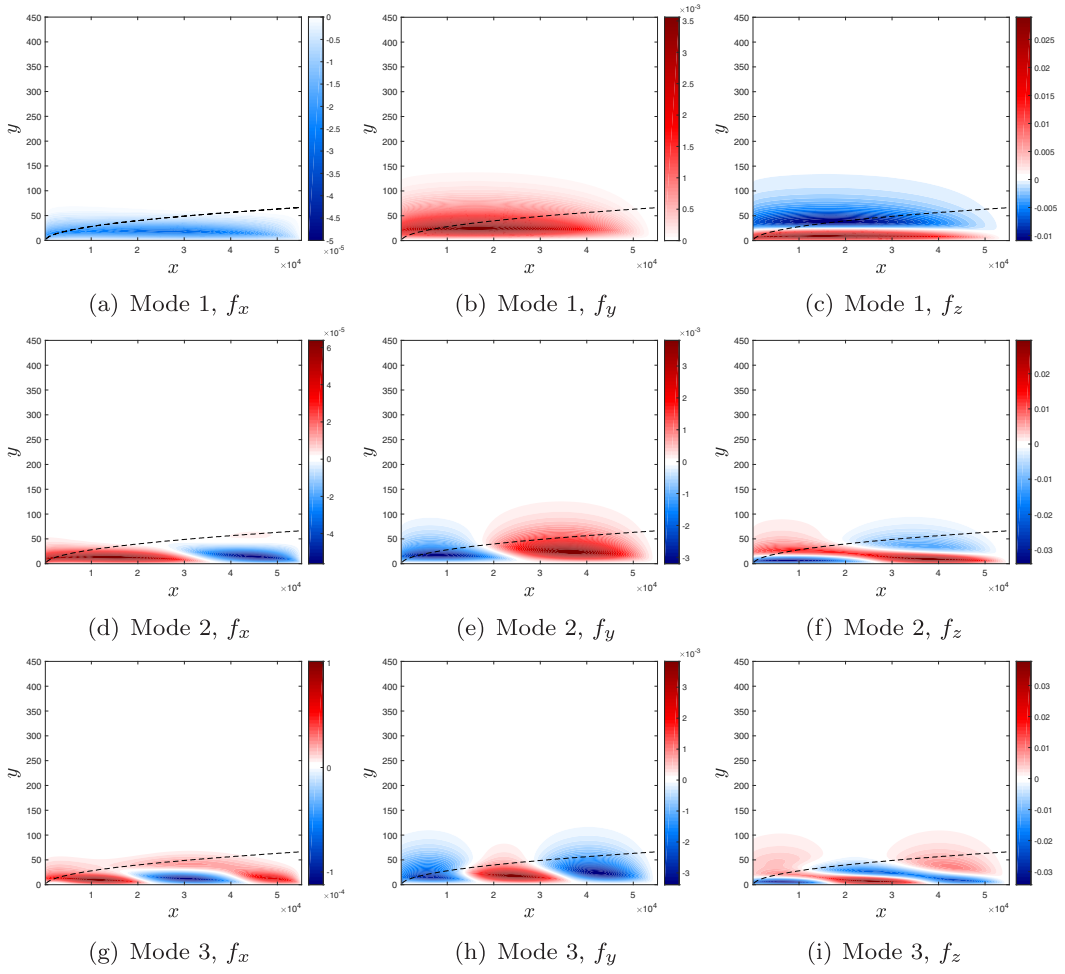

(a) Mode 1, f_x (b) Mode 1, f_y (c) Mode 1, f_z

(d) Mode 2, f_x (e) Mode 2, f_y (f) Mode 2, f_z

(g) Mode 3, f_x (h) Mode 3, f_y (i) Mode 3, f_z

FIG. 8. Shape of the three most amplified forces in the wall-normal and streamwise direction for f_x, f_y, and f_z, and Re = 7000, with $(\omega, \beta) = (0, 0.04)$. The dashed line indicates the boundary-layer thickness.

with those predicted from an optimal perturbation analysis [28,30,31], the receptivity between the free-stream disturbances and their effect inside the boundary layer is not yet fully understood [21].

The results of Figs. 8 and 9 indicate that streaky structures occurring inside the boundary layer result from the optimal forcing which extends throughout the streamwise direction and up to the free-stream region in the wall-normal direction. The receptivity mechanism can therefore be related to such optimal forcing. In order to assess the effect of a force which is limited to the free-stream region, in an idealized scenario for free-stream turbulence fluctuations, we add a restriction to the force, limiting it to be outside of the boundary layer. Since we are only interested in the optimal forcing, we here consider Eq. (38), for the steepest descent method, multiplying the gradient by $W_{bl}^{n_x \times n_y}$, a matrix which is zero for points inside the boundary layer and one for points outside of it. The resulting (restricted) optimal force and response are shown in Fig. 12 along with the behavior of the total kinetic energy in the streamwise direction for Re = 7000, $\beta = 0.04$, $\omega = 0$, and the $\beta -$ Re parametric study for the zero-pressure-gradient case; similar observations were also made for the other pressure gradients evaluated.

We observe that the restricted force results in fluctuations similar in shape to those of the optimal force, i.e., streaky structures which grow along the streamwise direction. As expected, the

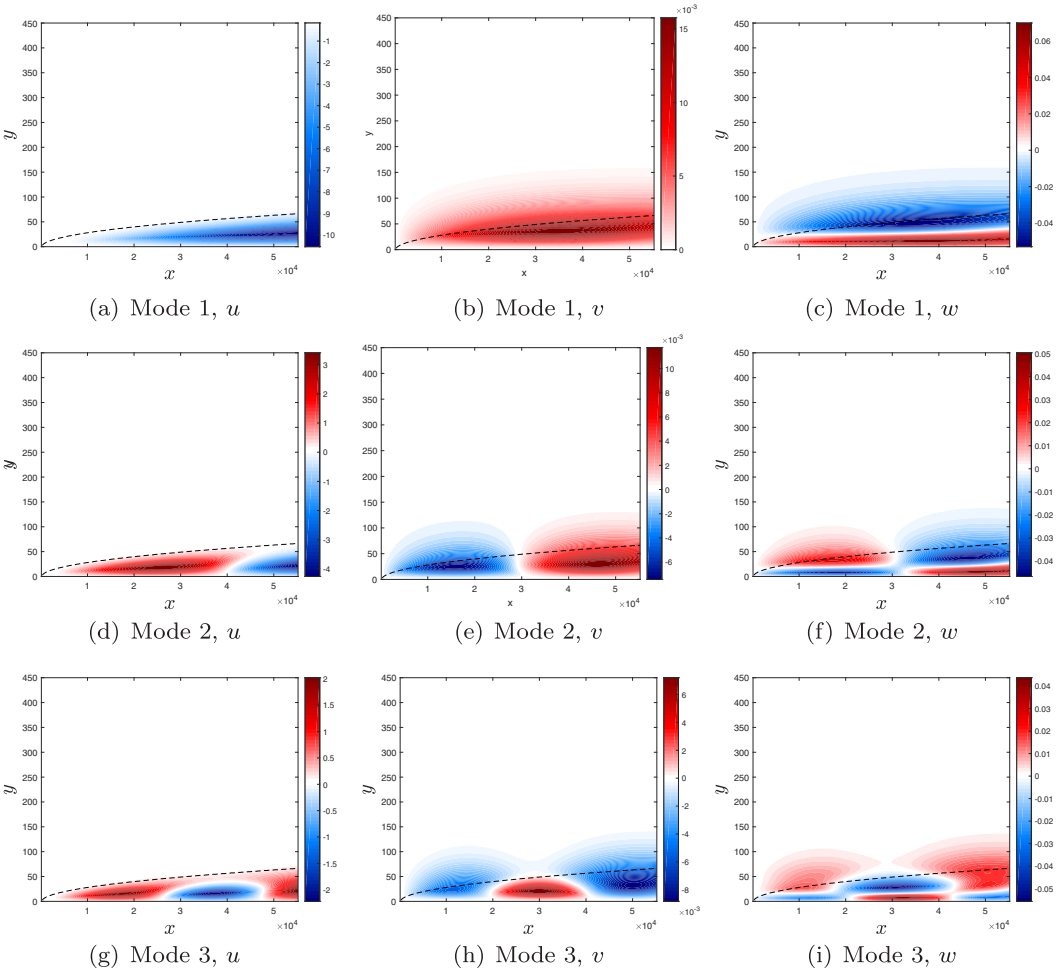

(a) Mode 1, u (b) Mode 1, v (c) Mode 1, w

(d) Mode 2, u (e) Mode 2, v (f) Mode 2, w

(g) Mode 3, u (h) Mode 3, v (i) Mode 3, w

FIG. 9. Shape of the three most amplified responses in the streamwise and wall-normal direction for u, v, and w, and $\mathrm{Re} = 7000$, with $(\omega, \beta) = (0, 0.04)$. The dashed line indicates the boundary-layer thickness.

resulting kinetic energy is lower than that of the optimal (unrestricted) force. The $\beta - \mathrm{Re}$ parametric study indicates that the most amplified β is smaller than for the corresponding unrestricted force, which in turn is associated to larger structures; however, the $1/\mathrm{Re}$ tendency is also observed here. These results help shed a light on the transition associated to the structures induced by free-stream turbulence, indicating that a force limited to the free-stream region is capable of generating streaky structures inside the boundary layer, which are the initial trigger for bypass transition. On the scenario of free-stream turbulence, the actual forcing present in the flow would present a nonzero projection on the optimal forcing, which extends up to the free-stream region, therefore leading to the appearance of the streaky structures in the flow. Furthermore, even though the amplitude of the forcing in the free stream is expected to be small at the component corresponding to α and ω equal zero, and the oblique mechanism [55] could generate such a mode, making it more relevant.

VI. RESOLVENT ANALYSIS OF A TURBULENT BOUNDARY LAYER

We start by computing the optimal force and response for range of spanwise wave numbers and Reynolds numbers, where the Reynolds number on the beginning of the domain is fixed at

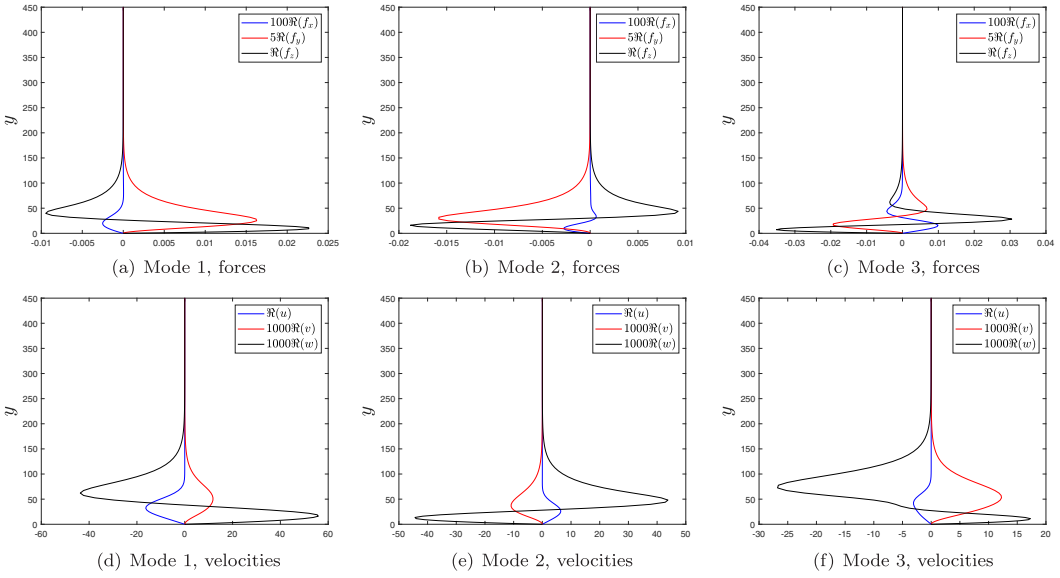

(a) Mode 1, forces (b) Mode 2, forces (c) Mode 3, forces

(d) Mode 1, velocities (e) Mode 2, velocities (f) Mode 3, velocities

FIG. 10. Envelope of the forces and velocities for the three first modes, at $x = 27\,000$ and $\mathrm{Re} = 7000$, for $(\omega, \beta) = (0, 0.04)$. Note that the v/w and f_y/f_z components have been multiplied by a constant factor, which is given in the legends, in order to enable the comparisons to be made in a single plot.

$\mathrm{Re} = 10\,000$, which is equivalent to $\mathrm{Re}_\theta = 7385$, defined in terms of the momentum thickness, $\mathrm{Re}_\theta = U_\infty \theta/\nu$. Here, the eddy viscosity model, computed following the approach described in Sec. III B, is considered. As before, only slow streamwise variations, captured by the envelope function $\hat{\mathbf{q}}(x, y, \beta, \omega)$ in Eq. (10), can be considered by this method, and they are the most amplified ones [47]. Only the $\omega = 0$ case is considered as it also corresponds to the most amplified frequency. In this section, only the parabolic resolvent calculation is considered as the same computations

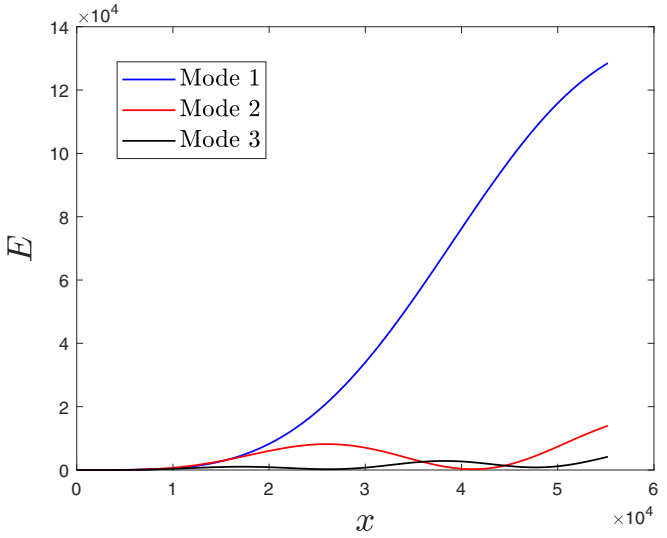

FIG. 11. Kinetic energy along the streamwise direction for the first three modes for the zero pressure gradient boundary layer of $\mathrm{Re} = 7000$, for $(\omega, \beta) = (0, 0.04)$.

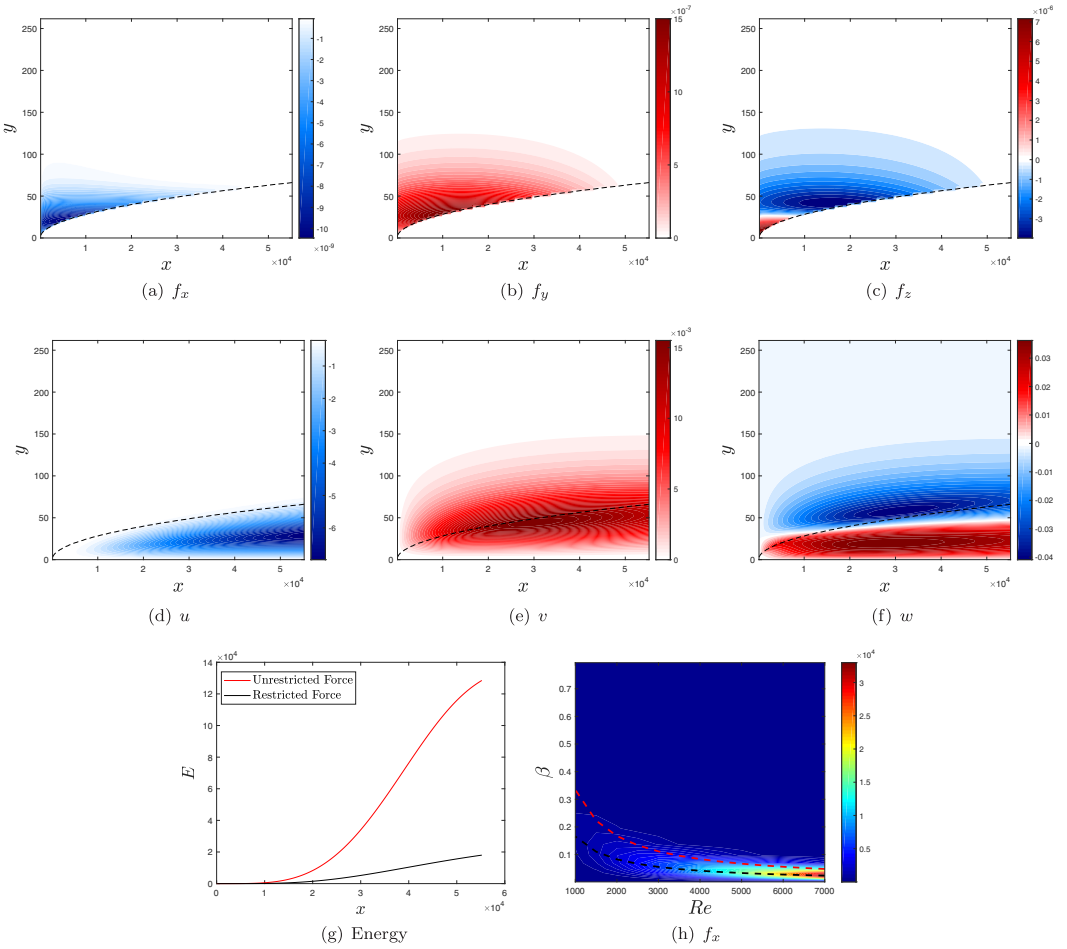

FIG. 12. Resulting optimal force [(a)–(c)], response [(d)–(f)]. Kinetic energy of the fluctuations compared to the unrestricted case (g), for Re $= 7000$, $\beta = 0.04$, $\omega = 0$, and $\beta -$ Re parametric study when the forcing location is restricted to the free stream (h). In subplot (h), the dashed black and red lines indicate the most amplified β for the restricted and unrestricted forces, respectively.

with the global approach would be much more computationally costly due to the number of points necessary to resolve the eddy viscosity in the wall-normal direction and higher Reynolds numbers used. The dominant eigenvalues are shown in Fig. 13 as a function of the spanwise wavelength, both in the outer and inner scales, $\lambda_z = 2\pi/\beta$ and $\lambda_z^+ = (2\pi/\beta)(\mathrm{Re}/U_e^+)$, respectively, and the eigenvalues have also been premultiplied either by β or β^+, as usual in wall-bounded turbulence [66]. We also show the behavior of the premultipled eigenvalues when considering the modified Rotta-Clauser parameter, $\Delta_\theta = \theta U_\infty/u_\tau$, as the characteristic length scale, as in Cossu *et al.* [47]. For completeness, the behavior of the suboptimal modes is included in Appendix B.

For the nonpremultiplied case, the spectrum presents a single peak, corresponding to the outer peak. For the premultiplied case, a second (inner) peak appears and is less sensitive to Reynolds number variations, as previously shown in Ref. [1]. For all the Reynolds numbers evaluated, when scaled in viscous units, the inner peak is observed to occur at $\lambda_z^+ \approx 80$, in accordance with previous evaluations for this flow [47]. The double peak structure is similar to that observed in other works [48,67,68], and characteristic of high-Reynolds turbulent flows. The outer peak presents increasing eigenvalues with the Reynolds number of the flow and it also moves toward larger

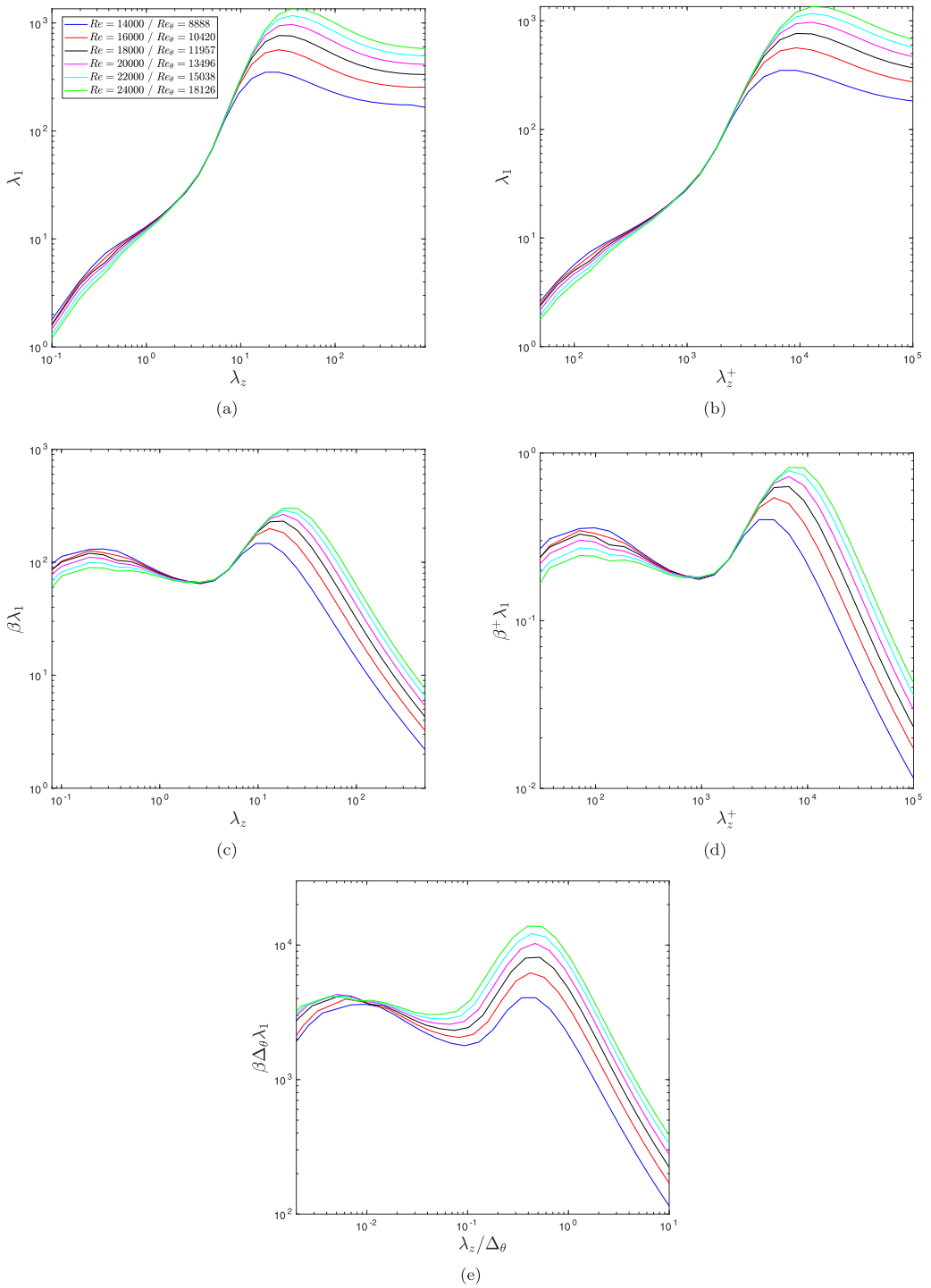

FIG. 13. Dominant eigenvalues computed for a turbulent boundary layer with eddy viscosity for different Reynolds numbers as a function of the spanwise wavelength, for $\omega = 0$. The eigenvalues have been pre-multiplied by β/β^+ in panels (c) and (d), respectively. In panel (e), the modified Rotta-Clauser parameter is considered as the characteristic length scale and the eigenvalues are premultiplied by $\beta\Delta_\theta$.

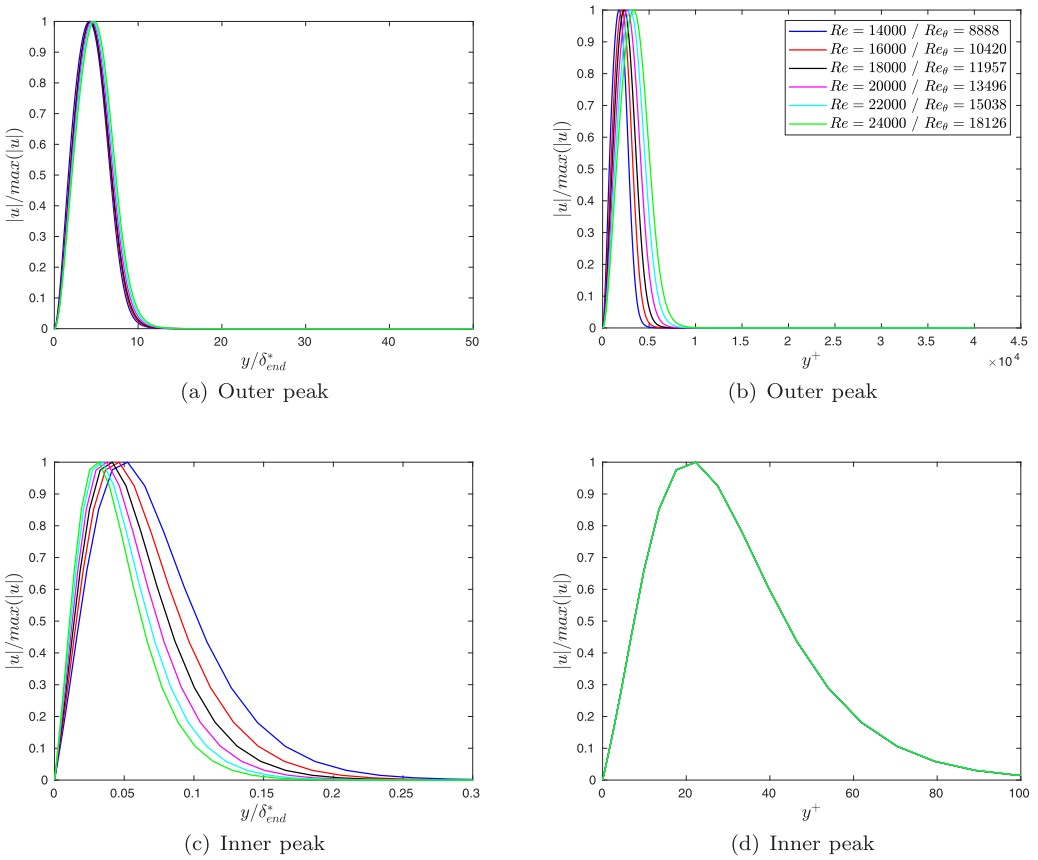

(a) Outer peak (b) Outer peak

(c) Inner peak (d) Inner peak

FIG. 14. Outer [(a), (b)] and inner [(c), (d)] peak streamwise velocity fluctuations for the Reynolds numbers evaluated. In panels (a) and (c), the wall-normal coordinate is nondimensionalized with the displacement thickness on the end of the computational domain and in panels (b) and (d), the viscous length scale is considered. The horizontal axis in the plots has been adjusted for each case in order to facilitate the evaluation of the results.

(higher λ_z) structures. As in Ref. [47], it is observed that the modified Rotta-Clauser length given by $\Delta_\theta = \theta U_\infty / u_\tau$ may be used as an approximate characteristic length scale for the flow, where the maximum wavelength, when scaled by this parameter, may be obtained from $\lambda_{z_{\max}}/\Delta_\theta \approx 0.4$, and equivalently, when written in terms of the boundary layer thickness, the outer peak occurs at $\beta\delta_{99} \approx 1$, in accordance with previous studies of turbulent boundary layer flows [69].

Figure 14 presents the streamwise velocity fluctuations at the outer and inner peaks for all the Reynolds numbers evaluated. We observe that the position of the maximum coalesces when the outer (viscous) length scales are used for the outer (inner) peak fluctuations, where the displacement thickness on the end of the domain may be used as the characteristic length scale for the outer peak fluctuations. Although not shown, the maxima also coalesce for the outer peak fluctuations when the modified Rotta-Clauser parameter is taken as the characteristic length scale.

Similarly to the analysis in Sec. V A, we consider a fixed streamwise domain and evaluate the effect of the Reynolds number on the amplification of the dominant gain for three Reynolds numbers, Re = 20 000, 24 000, and 29 500. The dominant gain as a function of β is shown in Fig. 15, where it has been normalized by the fourth power of a modified Reynolds number, defined

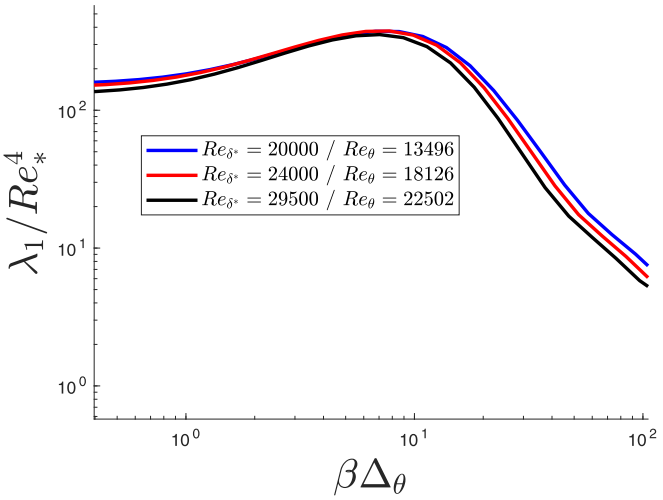

FIG. 15. Dominant gain, corresponding to the outer peak, scaled with Re_*^4 for three Reynolds numbers with the same streamwise domain as a function of $\beta\Delta_\theta$.

as per Ref. [47], as $\mathrm{Re}_* = U_\infty \Delta_\theta / \nu_{T_{\max}}$, where $\nu_{T_{\max}}$ corresponds to the maximum value of the total viscosity. Similarly to the laminar case, the gains scale with the fourth power of a modified Reynolds number. Although there is no clear choice of scaling parameters for a spatially developing turbulent boundary layer, the use of the maximum turbulent viscosity and the Rotta-Clauser parameter causes the gains to coalesce, indicating that the outer peak is also Reynolds independent. The wave number of the peak is also observed to coalesce, occurring at $\beta\Delta_\theta \approx 10$ for all the evaluated cases, when the streamwise domain is fixed and the data are not premultiplied.

Figure 16 presents the behavior of the optimal velocity fluctuations at the inner and outer peaks for the case of $\mathrm{Re} = 14\,000$ ($\mathrm{Re}_\theta = 8888$); similar results are observed for the other Reynolds numbers evaluated. In both cases, the optimal response consists of spanwise vortices (v and w) and

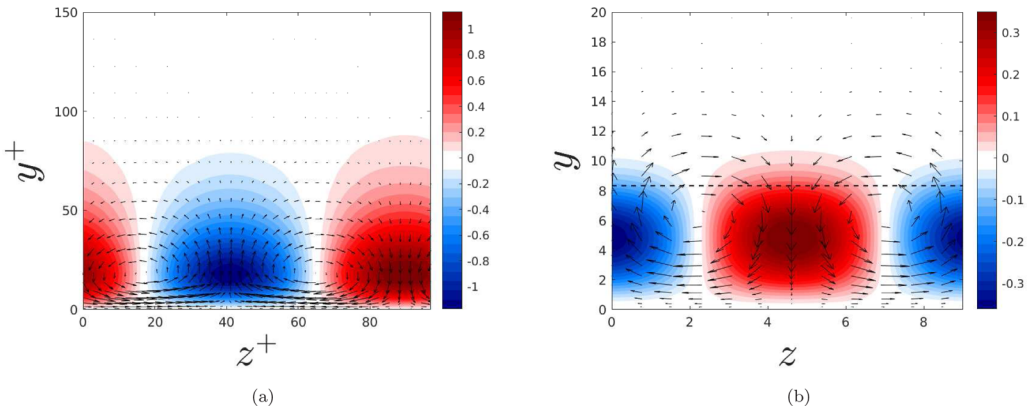

FIG. 16. Velocity fluctuations for the optimal response at the inner (a), in viscous units, and outer (b), in outer units, peaks for a turbulent boundary layer of $\mathrm{Re} = 14\,000$ ($\mathrm{Re}_\theta = 8888$). The color depicts the streamwise velocity and the arrows represent the vector field produced by the spanwise and wall-normal velocity components. In subplot (b), the dashed line indicates the boundary layer thickness.

streaks (u). The structures at the inner peak are centered at $y^+ \approx 10$, in accordance with other works [47,48]. The streamwise velocity fluctuations of the outer peak are centered inside the boundary layer whereas the streamwise vortices are at higher wall-normal positions with their center close to the boundary layer edge, as noted in Ref. [47].

VII. CONCLUSIONS

The resolvent formulation has become an important tool for applications in fluid mechanics, both for laminar and turbulent flows. Its input-output formulation, derived in the frequency domain, allows a simplified description of fluid problems, where the nonlinearities of the Navier-Stokes equations are replaced by a forcing to an otherwise linear operator, an approach which has led to several physical insights within the fluid mechanics community. The application of the resolvent approach for 1D (parallel) base flows is straightforward; nevertheless, the use for 2D or 3D problems is limited by computational constraints due to the resulting large matrices which need to be manipulated.

In this work, we developed a matrix-free approach for the optimization of the forcing, which is based on direct-adjoint iterations, derived from an optimization using the boundary-layer equations via the Lagrange multipliers method, which results in a parabolic resolvent calculation. The method is further combined with the Krylov-Arnoldi decomposition to enable the computation of suboptimal modes in a fast, computationally efficient manner. A comparison of the current approach against the more usual global resolvent method, using a LU decomposition for sparse matrices, demonstrates that more than one order of magnitude of reduction may be obtained in the computational cost and more than three orders of magnitude of reduction may be obtained for the memory requirements of the calculation, for the same accuracy of the results, thus making the method a promising approach for application in both laminar and turbulent high-Reynolds flows.

The use of the parabolic resolvent is exemplified for the Falkner-Skan boundary layer where we extend the results found in the literature for the optimal perturbation for the case of the optimal and suboptimal forcings for flows with pressure gradient. Trends for the resulting gain and optimal β are derived where higher Reynolds and adverse pressure gradients are associated to larger gains and smaller β values which, in turn, require larger wall-normal domains for adequate computations. We here extend the findings of Ref. [28] for boundary layers with pressure gradient via an optimal forcing calculation, where the optimal spanwise wave number is also observed to be proportional to $1/\mathrm{Re}$. We further note that the gains scale with Re^4 when the same streamwise domain is considered. It should be noted that the parametric studies involving β, ω, Re, and pressure gradient performed here would be much more costly computationally using the global resolvent approach, which could be prohibitive, depending on the application. We further highlight the importance of the work for free-stream turbulence receptivity. First we demonstrate that a forcing restricted to the free-stream region is able to generate streaky structures which would trigger transition downstream; the parametric study performed for this flow indicates the most amplified β is also proportional to $1/\mathrm{Re}$ but associated to smaller β and larger structures compared to the unrestricted case. Second we observe that the v and w fluctuations resulting from the optimal forcing grow along the streamvise direction, as they are continuously driven by the forcing components. Both of these features are believed to be related to a scenario involving free-stream turbulence transition and had not been yet reported.

Furthermore, the computations indicate that streaky structures, associated to $\omega = 0$ correspond to both optimal and suboptimal fluctuations where the suboptimals saturate at different streamwise positions. This trend, which had not yet been observed for the suboptimal modes, is thought to be related to the sensitivity of the optimal perturbation with respect to the position where it is generated. These results help shed a light in other studies, such as Ref. [31], where the difficulty in obtaining active flow control of streaky structures is associated to the inability of actuators in reproducing the optimal structure in the flow.

As outlined in the introduction, the resolvent method has become a tool of frequent use for the study of turbulent flows which could benefit from the current method, given its computational efficiency, which allows computations at very high Reynolds numbers, for flows with a streamwise variation. We present an example of application for a turbulent boundary layer, using the base flow described in Ref. [60], with the addition of a wall-normal direction-dependent eddy viscosity. Application of the parabolic resolvent for this flow leads to the appearance of two peaks in the premultiplied spectrum associated to inner and outer peak fluctuations. We are able to recover the scaling of the fluctuations in terms of viscous units and the Rotta-Clauser modified parameter or the displacement thickness as the relevant length scales for inner and outer fluctuations, respectively, which leads the resulting fluctuations to coalesce in the wall-normal direction. We further note that the outer peak gains scale similarly to the laminar boundary layer, with a modified Reynolds number to the fourth power, indicating that it is Reynolds independent. Finally, we note that streaks and streamwise vortices are the most amplified structures in this flow where, for outer layer structures, the vortices are centered close to the boundary layer edge with a significant support above it, akin to observations made for laminar boundary layers.

Finally, the method outlined in the current work is restricted to small values of ω. Analysis of cases with high values of ω would require the adaptation of the parabolized stability equations. Such a study, which is out of the scope of the current work, could be of relevance for aeroacoustics problems and the nonlinear interaction between oblique waves, for example, as both of these cases are associated to higher values of ω.

ACKNOWLEDGMENTS

A.V.G.C. was supported by CNPq Grant No. 313225/2020-6 and FAPESP Grant No. 2019/27655-3. The authors would also like to acknowledge the funding from Vinnova through their programs NFFP, Swedemo, and CISB (Swedish-Brazilian Research and Innovation Centre). Simulations have been performed at National Supercomputer Centre (NSC) and High Performance Computing Center North (HPC2N) with computer time provided by the Swedish National Infrastructure for Computing (SNIC). K.S. would like to acknowledge L.I. Abreu for the support regarding the turbulent boundary layer mean flow.

The authors declare that they have no conflict of interest.

APPENDIX A: TURBULENT BOUNDARY LAYER PROFILE

For the sake of completeness, the explicit expressions used for the turbulent boundary layer profile proposed in Ref. [60] are reported here:

$$U_w^+(\mu) = \left[\frac{1}{\kappa}E_1(\mu) + w_0\right]\frac{1}{2}\left[1 - \tanh\left(\frac{w_{-1}}{\mu} + w_2\mu^2 + w_8\mu^8\right)\right] \tag{A1}$$

where $w_0 = 0.6332$, $w_{-1} = -0.096$, $w_2 = 28.5$, $w_8 = 33\,000$, and

$$E_1(\mu) = -\gamma - \ln(\mu) + 0.99999193\mu - 0.24991055\mu^2 + 0.05519968\mu^3 - 0.00976004\mu^4 + 0.00107857\mu^5, \tag{A2}$$

with $\gamma = 0.57721566$, corresponding to the Euler constant. The other velocity components are then given as

$$U_{\log}^+(y^+) = \frac{1}{\kappa}\ln(y^+) + B, \tag{A3}$$

$$U_e^+(Re) = \frac{1}{\kappa}\ln(\mathrm{Re}) + C, \tag{A4}$$

where $\kappa = 0.384$, $B = 4.17$, and $C = 3.3$;

$$U_i^+(y^+) = 0.68285472\ln(y^{+^2} + 4.7673096y^+ + 9545.9963)$$

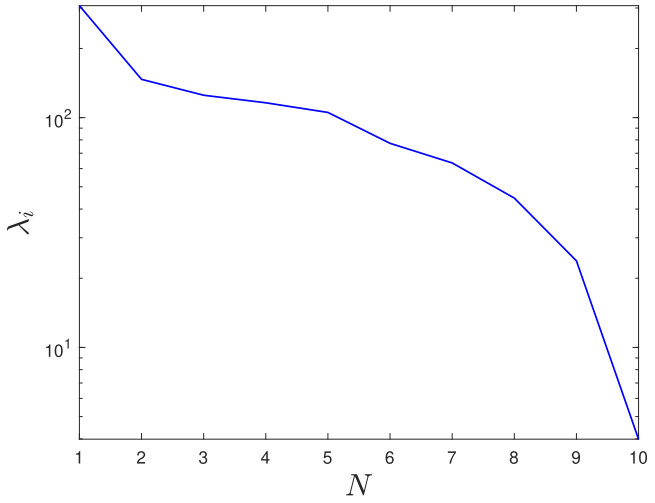

FIG. 17. Eigenvalues computed for a turbulent boundary layer of $\mathrm{Re} = 14\,000$ ($\mathrm{Re}_\theta = 8888$), for $\beta = 0.5$ and $\omega = 0$.

$$
\begin{aligned}
&+ 1.2408249 \arctan(0.01028083y^+ + 0.024404056)\\
&+ 1.2384572 \ln(y^+ + 95.232690) - 11.930683\\
&- 0.50435126 \ln(y^{+^2} - 7.8796955y^+ + 78.389178)\\
&+ 4.7413546 \arctan(0.12612158y^+ - 0.49689982)\\
&- 2.7768771 \ln(y^{+^2} + 16.209175y^+ + 933.16587)\\
&+ 0.37625729 \arctan(0.033952353y^+ + 0.27516982)\\
&+ 6.5624567 \ln(y^+ + 13.670520 + 6.1128254),
\end{aligned}
\tag{A5}
$$

where, as in the main document, the $+$ superscript refers to quantities which are nondimensionalized in inner variables, i.e., friction velocity and viscous length scale.

The x-dependent Reynolds number may be obtained as

$$
\mathrm{Re}_x = \mathrm{Re}_\theta\left(6.7817\ln^2(\mathrm{Re}_\theta) + 3.6241\ln(\mathrm{Re}_\theta) + 44.2971 + \frac{50.5521}{\ln(\mathrm{Re}_\theta)} + \frac{27.9533}{\ln^2(\mathrm{Re}_\theta)} - \frac{55.6211}{\ln^3(\mathrm{Re}_\theta)} - \frac{85.5817}{\ln^4(\mathrm{Re}_\theta)}\right). \tag{A6}
$$

From Re_x, the streamwise extent nondimensionalized by the momentum thickness is obtained from

$$
\frac{x}{\theta} = \left(\frac{\kappa^2}{\ln^2(\mathrm{Re}_x)} - \frac{\kappa^2\{4\ln(\kappa) - 2 + 2\kappa C - 4\ln[\ln(\mathrm{Re}_x)]\}}{\ln^3(Re_x)}\right)^{-1}. \tag{A7}
$$

The momentum thickness can be readily computed at each streamwise station and used to fix the nondimensionalization to the displacement thickness in the first point of the considered domain.

APPENDIX B: SUBOPTIMAL MODES FOR THE TURBULENT BOUNDARY LAYER PROFILE

For completeness, the optimal and suboptimal modes are presented here for the turbulent boundary layer case, computed via the parabolic resolvent approach. As in Sec. VI, the Reynolds number

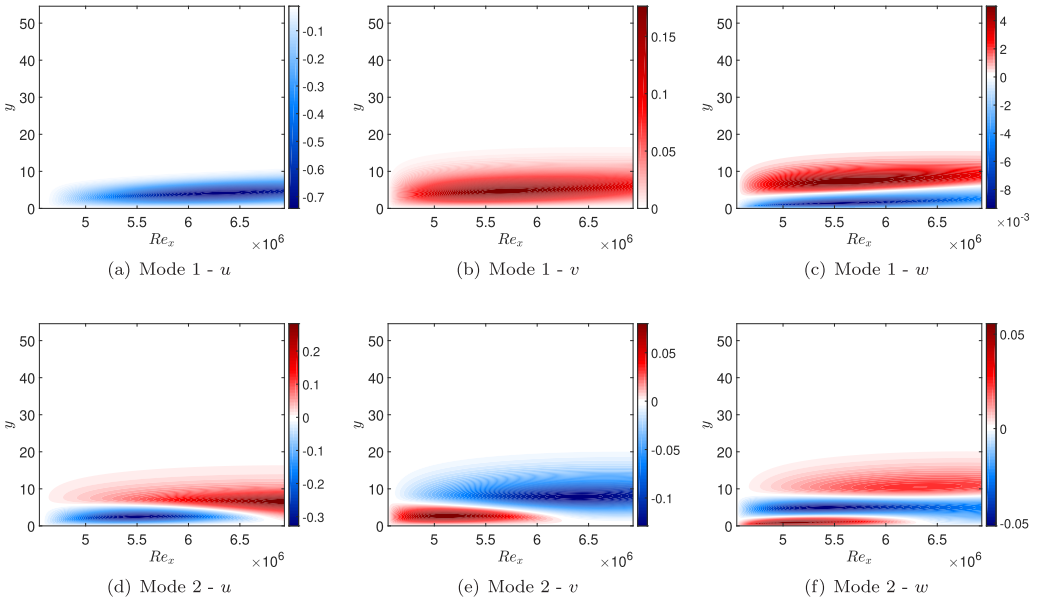

(a) Mode 1 - u (b) Mode 1 - v (c) Mode 1 - w

(d) Mode 2 - u (e) Mode 2 - v (f) Mode 2 - w

FIG. 18. Behaviour of the optimal [in panels (a)–(c)] and first suboptimal [in panels (d)–(f)] mode in the x-y plane for a turbulent boundary layer of $\mathrm{Re} = 14\,000$ ($\mathrm{Re}_\theta = 8888$), for $(\omega, \beta) = (0, 0.5)$ and the three velocity components.

on the beginning of the computational domain is $\mathrm{Re} = 10\,000$ ($\mathrm{Re}_\theta = 7385$) and the boundary layer extends up to $\mathrm{Re} = 14\,000$ ($\mathrm{Re}_\theta = 8888$); the spanwise wave number $\beta = 0.5$ is considered as a sample case. Similar trends are observed for other cases considered.

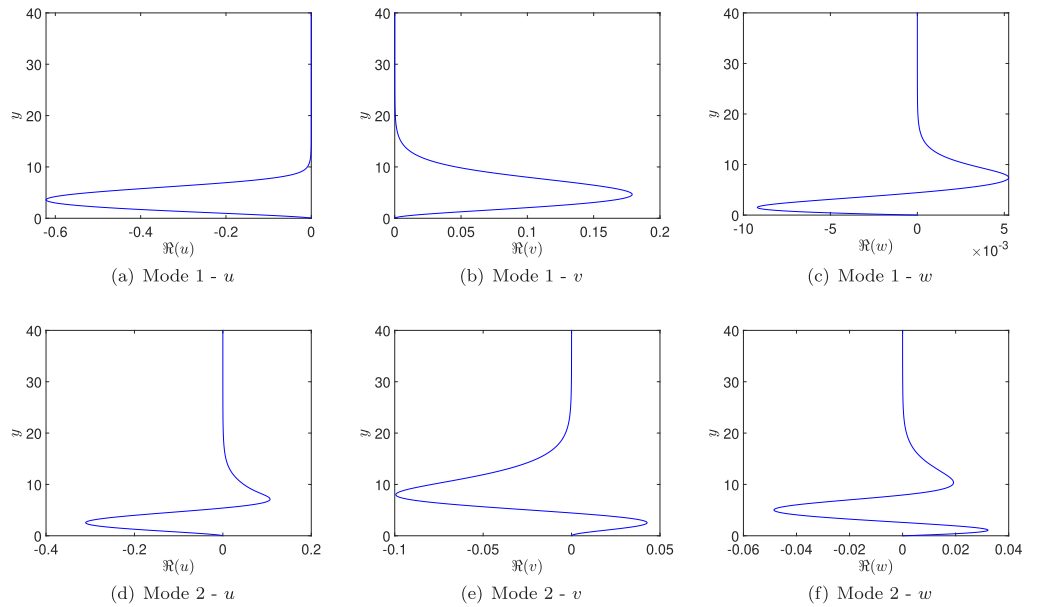

(a) Mode 1 - u (b) Mode 1 - v (c) Mode 1 - w

(d) Mode 2 - u (e) Mode 2 - v (f) Mode 2 - w

FIG. 19. Behavior of the optimal [in panels (a)–(c)] and first suboptimal [in panels (d)–(f)] mode in the wall-normal direction for a turbulent boundary layer of $\mathrm{Re} = 14\,000$ ($\mathrm{Re}_\theta = 8888$), for $(\omega, \beta) = (0, 0.5)$ and the three velocity components.

Figure 17 presents the 10 first eigenvalues, confirming the strong dominance of the first mode. The optimal and first suboptimal are shown in Fig. 18, in the x-y plane, and the corresponding behavior along the wall-normal direction is given in Fig. 19.

[1] Y. Hwang and C. Cossu, Linear non-normal energy amplification of harmonic and stochastic forcing in turbulent channel flow, J. Fluid Mech. **664**, 51 (2010).

[2] B. J. McKeon, The engine behind (wall) turbulence: Perspectives on scale interactions, J. Fluid Mech. **817**, 1 (2017).

[3] B. J. McKeon and A. S. Sharma, A critical-layer framework for turbulent pipe flow, J. Fluid Mech. **658**, 336 (2010).

[4] B. F. Farrell and P. J. Ioannou, Stochastic forcing of the linearized Navier-Stokes equations, Phys. Fluids A: Fluid Dyn. **5**, 2600 (1993).

[5] P. J. Schmid, Nonmodal stability theory, Annu. Rev. Fluid Mech. **39**, 129 (2007).

[6] P. J. Schmid and D. S. Henningson, *Stability and Transition in Shear Flows*, Applied Mathematical Sciences (Springer Science & Business Media, Berlin, 2012), Vol. 142.

[7] G. Tissot, M. Zhang, F. C. Lajús Jr., A. V. G. Cavalieri, and P. Jordan, Sensitivity of wave packets in jets to nonlinear effects: The role of the critical layer, J. Fluid Mech. **811**, 95 (2017).

[8] L. N. Trefethen, A. E. Trefethen, S. C. Reddy, and T. A. Driscoll, Hydrodynamic stability without eigenvalues, Science **261**, 578 (1993).

[9] L. Lesshafft, O. Semeraro, V. Jaunet, A. V. G. Cavalieri, and P. Jordan, Resolvent-based modeling of coherent wave packets in a turbulent jet, Phys. Rev. Fluids **4**, 063901 (2019).

[10] A. Towne, O. T. Schmidt, and T. Colonius, Spectral proper orthogonal decomposition and its relationship to dynamic mode decomposition and resolvent analysis, J. Fluid Mech. **847**, 821 (2018).

[11] P. A. S. Nogueira, A. V. G. Cavalieri, P. Jordan, and V. Jaunet, Large-scale streaky structures in turbulent jets, J. Fluid Mech. **873**, 211 (2019).

[12] L. I. Abreu, A. V. G. Cavalieri, P. Schlatter, R. Vinuesa, and D. S. Henningson, Spectral proper orthogonal decomposition and resolvent analysis of near-wall coherent structures in turbulent pipe flows, J. Fluid Mech. **900**, A11 (2020).

[13] A. Sano, L. I. Abreu, A. V. G. Cavalieri, and W. R. Wolf, Trailing-edge noise from the scattering of spanwise-coherent structures, Phys. Rev. Fluids **4**, 094602 (2019).

[14] M. Luhar, A. S. Sharma, and B. J. McKeon, Opposition control within the resolvent analysis framework, J. Fluid Mech. **749**, 597 (2014).

[15] S. Beneddine, R. Yegavian, D. Sipp, and B. Leclaire, Unsteady flow dynamics reconstruction from mean flow and point sensors: An experimental study, J. Fluid Mech. **824**, 174 (2017).

[16] E. Martini, A. Cavalieri, P. Jordan, A. Towne, and L. Lesshafft, Resolvent-based optimal estimation of transitional and turbulent flows. Journal of Fluid Mechanics, J. Fluid Mech. **900**, A2 (2022).

[17] A. Towne, A. Lozano-Durán, and X. Yang, Resolvent-based estimation of space-time flow statistics, J. Fluid Mech. **883**, A17 (2020).

[18] P. Morra, P. A. S. Nogueira, A. V. G. Cavalieri, and D. S. Henningson, The colour of forcing statistics in resolvent analyses of turbulent channel flows, J. Fluid Mech. **907**, A24 (2021).

[19] P. A. S. Nogueira, P. Morra, E. Martini, A. V. G. Cavalieri, and D. S. Henningson, Forcing statistics in resolvent analysis: Application in minimal turbulent Couette flow, J. Fluid Mech. **908**, A32 (2021).

[20] O. Kaplan, P. Jordan, A. V. G. Cavalieri, and G. A. Brès, Nozzle dynamics and wave packets in turbulent jets, J. Fluid Mech. **923**, A22 (2021).

[21] J. H. M. Fransson and S. Shahinfar, On the effect of free-stream turbulence on boundary-layer transition, J. Fluid Mech. **899**, A23 (2020).

[22] M. Matsubara and P. H. Alfredsson, Disturbance growth in boundary layers subjected to free-stream turbulence, J. Fluid Mech. **430**, 149 (2001).

[23] K. J. A. Westin, A. V. Boiko, B. G. B. Klingmann, V. V. Kozlov, and P. H. Alfredsson, Experiments in a boundary layer subjected to free stream turbulence. Part 1. Boundary layer structure and receptivity, J. Fluid Mech. **281**, 193 (1994).
[24] T. A. Zaki, From streaks to spots and on to turbulence: Exploring the dynamics of boundary layer transition, Flow, Turbul. Combust. **91**, 451 (2013).
[25] T. A. Zaki and P. A. Durbin, Mode interaction and the bypass route to transition, J. Fluid Mech. **531**, 85 (1999).
[26] L. S. Hultgren and L. H. Gustavsson, Algebraic growth of disturbances in a laminar boundary layer, Phys. Fluids **24**, 1000 (1981).
[27] T. A. Zaki and S. Saha, On shear sheltering and the structure of vortical modes in single-and two-fluid boundary layers, J. Fluid Mech. **626**, 111 (2009).
[28] P. Andersson, M. Berggren, and D. S. Henningson, Optimal disturbances and bypass transition in boundary layers, Phys. Fluids **11**, 134 (1999).
[29] O. Levin and D. S. Henningson, Exponential vs algebraic growth and transition prediction in boundary layer flow, Flow, Turbul. Combust. **70**, 183 (2003).
[30] P. Luchini, Reynolds-number-independent instability of the boundary layer over a flat surface: Optimal perturbations, J. Fluid Mech. **404**, 289 (2000).
[31] K. Sasaki, P. Morra, A. V. G. Cavalieri, A. Hanifi, and D. S. Henningson, On the role of actuation for the control of streaky structures in boundary layers, J. Fluid Mech. **883**, A34 (2020).
[32] M. R. Jovanović and B. Bamieh, Componentwise energy amplification in channel flows, J. Fluid Mech. **534**, 145 (2005).
[33] P. A. S. Nogueira, A. V. G. Cavalieri, A. Hanifi, and D. S. Henningson, Resolvent analysis in unbounded flows: Role of free-stream modes, Theor. Comput. Fluid Dyn. **34**, 163 (2020).
[34] O. T. Schmidt, A. Towne, G. Rigas, T. Colonius, and G. A. Brès, Spectral analysis of jet turbulence, J. Fluid Mech. **855**, 953 (2018).
[35] D. Sipp and O. Marquet, Characterization of noise amplifiers with global singular modes: The case of the leading-edge flat-plate boundary layer, Theor. Comput. Fluid Dyn. **27**, 617 (2013).
[36] M. Brynjell-Rahkola, L. S. Tuckerman, P. Schlatter, and D. S. Henningson, Computing optimal forcing using Laplace preconditioning, Commun. Comput. Phys. **22**, 1508 (2017).
[37] F. Gómez, H. M. Blackburn, M. Rudman, A. S. Sharma, and B. J. McKeon, A reduced-order model of three-dimensional unsteady flow in a cavity based on the resolvent operator, J. Fluid Mech. **798**, R2 (2016).
[38] A. Monokrousos, E. Åkervik, L. Brandt, and D. S. Henningson, Global three-dimensional optimal disturbances in the Blasius boundary-layer flow using time-steppers, J. Fluid Mech. **650**, 181 (2010).
[39] E. Martini, D. Rodríguez, A. Towne, and A. V. G. Cavalieri, Efficient computation of global resolvent modes, J. Fluid Mech. **919**, A3 (2021).
[40] A. Hanifi, P. J. Schmid, and D. S. Henningson, Transient growth in compressible boundary layer flow, Phys. Fluids **8**, 826 (1996).
[41] D. Tempelmann, A. Hanifi, and D. S. Henningson, Spatial optimal growth in three-dimensional boundary layers, J. Fluid Mech. **646**, 5 (2010).
[42] G. Rigas, O. Kamal, A. Towne, and T. Colonius, Efficient global resolvent analysis via the one-way Navier-Stokes equations. Part 2. Optimal response, arXiv:2111.09273.
[43] A. Towne, G. Rigas, E. Pickering, and T. Colonius, Efficient global resolvent analysis via the one-way Navier-Stokes equations. Part 1. Forced response, J. Fluid. Mech. **948**, A9 (2022).
[44] J. H. M. Ribeiro, C. Yeh, and K. Taira, Randomized resolvent analysis, Phys. Rev. Fluids **5**, 033902 (2020).
[45] B. Barthel, S. Gomez, and B. J. McKeon, Variational formulation of resolvent analysis, Phys. Rev. Fluids **7**, 013905 (2022).
[46] F. Li and M. R. Malik, On the nature of PSE approximation, Theor. Comput. Fluid Dyn. **8**, 253 (1996).
[47] C. Cossu, G. Pujals, and S. Depardon, Optimal transient growth and very large-scale structures in turbulent boundary layers, J. Fluid Mech. **619**, 79 (2009).

[48] J. C. del Álamo and J. Jimenez, Linear energy amplification in turbulent channels, J. Fluid Mech. **559**, 205 (2006).
[49] P. Morra, O. Semeraro, D. S. Henningson, and C. Cossu, On the relevance of Reynolds stresses in resolvent analyses of turbulent wall-bounded flows, J. Fluid Mech. **867**, 969 (2019).
[50] W. C. Reynolds and W. G. Tiederman, Stability of turbulent channel flow, with application to Malkus's theory, J. Fluid Mech. **27**, 253 (1967).
[51] W. C. Reynolds and A. K. M. F. Hussain, The mechanics of an organized wave in turbulent shear flow. Part 3. Theoretical models and comparisons with experiments, J. Fluid Mech. **54**, 263 (1972).
[52] S. Symon, A. Madhusudanan, S. J. Illingworth, and I. Marusic, On the use of eddy viscosity in resolvent analysis of turbulent channel flow, arXiv:2205.11216.
[53] F. P. Bertolotti and T. Herbert, Analysis of the linear stability of compressible boundary layers using the PSE, Theor. Comput. Fluid Dyn. **3**, 117 (1991).
[54] T. Herbert, Parabolized stability equations, Annu. Rev. Fluid Mech. **29**, 245 (1997).
[55] S. Berlin and D. S. Henningson, A nonlinear mechanism for receptivity of free-stream disturbances, Phys. Fluids **11**, 3749 (1999).
[56] L. Brandt, D. S. Henningson, and D. Ponziani, Weakly nonlinear analysis of boundary layer receptivity to free-stream disturbances, Phys. Fluids **14**, 1426 (2002).
[57] J. O. Pralits, C. Airiau, A. Hanifi, and D. S. Henningson, Sensitivity analysis using adjoint parabolized stability equations for compressible flows, Flow, Turbulence Combust. **65**, 321 (2000).
[58] Y. Saad, *Iterative Methods for Sparse Linear Systems* (SIAM, Minneapolis, Minnesota, 2003).
[59] H. Schlichting, *Boundary Layer Theory*, 7th ed. (McGraw Hill, Berlin, 1968), Vol. 960.
[60] P. A. Monkewitz, K. A. Chauhan, and H. M. Nagib, Self-consistent high-Reynolds-number asymptotics for zero-pressure-gradient turbulent boundary layers, Phys. Fluids **19**, 115101 (2007).
[61] R. B. Lehoucq and D. C. Sorensen, Deflation techniques for an implicitly restarted Arnoldi iteration, SIAM J. Matrix Anal. Appl. **17**, 789 (1996).
[62] L. Brandt, The lift-up effect: The linear mechanism behind transition and turbulence in shear flows, Eur. J. Mech. B Fluids **47**, 80 (2014).
[63] T. Ellingsen and E. Palm, Stability of linear flow, Phys. Fluids **18**, 487 (1975).
[64] M. T. Landahl, A note on an algebraic instability of inviscid parallel shear flows, J. Fluid Mech. **98**, 243 (1980).
[65] S. C. Reddy and D. S. Henningson, Energy growth in viscous channel flows, J. Fluid Mech. **252**, 209 (1993).
[66] N. Hutchins and I. Marusic, Evidence of very long meandering features in the logarithmic region of turbulent boundary layers, J. Fluid Mech. **579**, 1 (2007).
[67] E. Dogan, R. Örlü, D. Gatti, R. Vinuesa, and P. Schlatter, Quantification of amplitude modulation in wall-bounded turbulence, Fluid Dyn. Research **51**, 011408 (2019).
[68] K. Sasaki, R. Vinuesa, A. V. G. Cavalieri, P. Schlatter, and D. S. Henningson, Transfer functions for flow predictions in wall-bounded turbulence, J. Fluid Mech. **864**, 708 (2019).
[69] G. Eitel-Amor, R. Örlü, and P. Schlatter, Simulation and validation of a spatially evolving turbulent boundary layer up to $\mathrm{Re}\theta = 8300$, Int. J. Heat Fluid Flow **47**, 57 (2014).